A Novel Transient Thermal Analysis of Direct Steam Generation External Receivers in Solar Power Tower Plants under Atmospheric Conditions Fluctuations

Hayder Al-Sarraf [1]
Department of Mechanical Engineering, Auckland University of Technology
Auckland, 1142, New Zealand
hayder.al-sarraf@autuni.ac.nz
ASME Membership (20103801387)

Ahmed Alhusseny
Department of Mechanical Engineering, Faculty of Engineering, University of Kufa
Najaf, 54003, Iraq
ahmedn.alhusseini@uokufa.edu.iq
Department of Mechanical and Aerospace Engineering, University of Manchester
Manchester, M13 9PL, UK
ahmed.alhusseny@manchester.ac.uk

Ramon Zamora
Department of Electrical Engineering, Auckland University of Technology
Auckland, New Zealand
ramon.zamora@aut.ac.nz

ABSTRACT

Solar power tower plants are leading candidates for electric power generation. They concentrate solar thermal power to heat the working medium used in the power cycle. However, atmospheric effects cause spatial and temporal fluctuations in solar thermal power during the day. Thus, evaluating the net power acquired by solar receiver tubes as a function of time and location is of high interest. A thorough dynamic thermal analysis procedure is developed in this research and examined under realistic weather conditions to demonstrate its potential for managing complex computations thoroughly and

[1] Corresponding author

cost-effectively. This research integrates high-accuracy solar field simulations by the SolarPILOT tool. In addition, a quasi-transient 1-D numerical simulation is implemented to predict the net heat flux and tube wall temperatures. The Kandlikar model is used to precisely characterize biphasic flow boiling inside receiver tubes. The current analysis is limited by its dependence on a 1-D axisymmetric approximation and natural convection heat losses. Three operational scenarios regarding their impact on the steam bulk temperature, productivity, and enthalpy in the Ivanpah I plant are discussed. One of the scenarios outperforms in net productivity due to the lower overall makeup required throughout the day, enabling the receiver to meet 93.61% of the plant steam demand in standalone mode, compared to 90.44% and 89.06% when the other two scenarios are followed. From a safe-operational point of view, tube wall temperature in the upper part of the receiver facing north, east, and west exceeds the maximum allowable limit. To address this issue, a mass flow interchange approach with optimal circulation factors between the opposing sides is proposed using a temperature control valve. It was found that the uneven distribution of steam fed to the superheater sides not only ensures the receiver's safety but also slightly reduces the total makeup required while increasing the excess energy available.

Keywords: solar power tower, direct steam generation, external receiver, weather conditions variations, SolarPILOT, transient thermal analysis.

1- INTRODUCTION

Among renewable energy sources, solar energy holds a prominent rank due to its ability to achieve environmental, economic, and safety objectives [1]. Quantitatively, around four quadrillion kWh of solar irradiance reaches the Earth's surface annually [2], which is significantly greater than the power demanded by the global population [3]. Even though such power is abundant and available, the low density and intermittence of solar energy embody significant shortcomings. The latter occurs due to attenuation and scattering through the atmosphere and cloudiness, making it less efficient. Therefore,

solar concentrators have been created to obtain high solar thermal energy [4–6]. Concentrating solar thermal collectors can deliver a high concentration ratio since the collector area is much larger than the receiver area and can track the sun from sunrise to sunset. Plants employing concentrating thermal collectors are known as concentrating solar power (CSP) plants. They represent an advanced solution to obtain applicable solar thermal energy systems; hence, such technology has received increasing investment, specifically in areas characterized by high solar radiation [7].

Among the available CSP plants nowadays, solar power tower (SPT) plants stand out for their capability of achieving high temperatures and efficiency [8,9] as well as their ease of integration with traditional power plants [10]. Moreover, they can be constructed at any site worldwide as long as the direct irradiance level is sufficient to create the thermal energy required to operate such plants [11]. SPT plants comprise hundreds/thousands of reflecting mirrors, called “heliostats,” assembled in circular paths around a solar tower. The heliostat's function is to receive, concentrate, and reflect the incident thermal solar beam onto the solar receiver [12], as shown in **Fig. 1**. They can supply elevated levels of concentrated solar thermal power up to 1000 kW/m^2. Consequently, the heat transfer fluid (HTF) supplied at a high temperature would maximize plant efficiency.

Fig. 1

In SPT plants, the solar receiver is mounted on top of a tower built in the center of the plant [13–15]. It acts as a heat exchanger, intercepting the reflected solar thermal power from heliostats. Then, an HTF circulating inside the solar receiver tubes absorbs

this thermal power through the tube walls. Finally, the thermal power absorbed by HTF is then utilized to run a Rankine cycle turbine and produce electric power. Based on their configuration, solar receivers are essentially classified into two kinds: cavity and external receivers. The two kinds have been used in SPT plants worldwide. However, several characteristics, such as simplicity in configuration, operation, maintenance, and transportation, make external receivers outperform cavity ones [16], and around 25% less area is required to absorb the same magnitude of thermal irradiance [16]. Nevertheless, previous research shows that external solar receivers have not been studied as extensively as cavity receivers, despite their aforementioned advantages [17]. In direct steam generation (DSG) technology, water vaporizes as it circulates through the receiver tubes. Therefore, it has drawn significant attention due to the following advantages: higher output temperature and thermal efficiency, simpler plant design, and lower initial cost [18–20].

The performance of SPT receivers is affected by weather conditions. Since solar radiation varies throughout the day, the heliostats reflect variable thermal flux accordingly. Also, the ambient temperature and wind velocity variations, which characterize thermal losses, are deemed key weather conditions that instantaneously affect the SPT receiver's performance. Rodríguez-Sánchez et al. [21] studied molten-salt-based external tubular receivers in SPT plants, considering variation in tube wall temperature in circumferential and axial directions under steady rather than transient thermal flux conditions. Liu et al. [22] proposed internally finned tubes for molten salt-based solar receivers to alleviate non-uniform heat distribution. In the investigation by

Crespi et al. [23], the performance of a molten salt SPT plant was examined under solar irradiance variability caused by cloud cover. However, only three different times were considered in the analysis. In the context of wind impact on receiver performance, convection thermal losses resulting from variations in wind speed and direction were investigated ([16], [24,25]). A recent scale analysis [26] has revealed that natural convection dominates and overrides forced convection in SPT receivers. So convective heat losses can be attributed solely to natural convection, significantly simplifying the analysis without compromising the accuracy of the targeted prediction.

Several simulation tools have been developed to simulate the concentrated sunrays incident on solar receivers. For example, the FluxSPT tool by Sánchez-González et al. [27] is used to depict the heliostat field and flux distribution on receiver tubes. However, such a tool cannot accommodate more than one direct normal irradiance (DNI) input. Also, its application is limited to specific receiver types and SPT plants. Another simulation software tool is the open-source SolarPILOT [28] established by the National Renewable Energy Laboratory (NREL). It can accommodate multiple DNI values simultaneously, enabling anticipation of the transient heat flux distribution on SPT receiver tubes during the daytime. This flexibility has led to the SolarPILOT software receiving increasing attention throughout the design and operation of the SPT plants. For instance, the numerical investigation conducted by Qaisrani et al. [25] concludes the performance and thermal efficiency of a DSG-based tubular external receiver under different wind velocities and directions. Nevertheless, this research still requires extension to evaluate the influence of the heat flux temporal variation during the day. SolarPILOT was also used

by Qaisrani et al. [16] to further examine the effects of wind on the thermal behavior of a rectangular external receiver. Nonetheless, only the receiver's north-facing side was investigated, neglecting the influence of the remaining sides (east, west, south) on the receiver's thermal behavior. Additionally, analyzing only a single DNI value is insufficient to estimate the receiver's performance.

As receiver productivity is expected to improve due to an increase in the number of heliostats, this may have two serious consequences. The first arises from an economic perspective, driven by the dramatic increase in capital costs. The second, from a safe-operation point of view, is due to the potential for generating extremely concentrated heat flux and its impact on the durability of the receiver structure. Bearing in mind that the long lifetime of the receiver would be affected by the long-lasting extreme temperatures of the tube wall while in operation, time-dependent deformation of the tube material is also expected to evolve. Therefore, operational safety issues have arisen while attempting to maximize the amount of concentrated solar heat incident on SPT receivers. In a related context, Rodríguez-Sánchez et al. [29] proposed a method to bypass the HTF between opposing receiver tubes exposed to instantaneously different levels of solar intensity. To do so, the panels located on opposite sides of the receiver are interconnected in a cross-over manner. The SPT receiver considered for the analysis was a cylindrical external receiver with molten-salt HTF, in which single- and multiple-flow patterns were investigated under the assumption of clear-sky conditions. Nevertheless, the authors did not account for DNI's transitory nature throughout the day, treating it as

a single value in their analysis. Furthermore, implementing such a remedy is quite hard and may considerably complicate the receiver design.

Although integrating DSG with external receivers offers performance and economic benefits, there is limited research on this promising combination. Furthermore, the impact of solar irradiation variability and realistic atmospheric conditions on steam production at the SPT plant has not yet been comprehensively investigated. Given the complexity and large scale of SPT plants, the existing simulation methods for assessing SPT performance are either complicated and computationally expensive or limited. Thus, the current research aims to bridge these knowledge gaps by establishing a simplified yet comprehensive approach that predicts the thermal performance of the DSG external receiver. This approach predicts the DSG external receiver's thermal performance, including steam temperature, quantity, enthalpy, and tube wall temperature, based on the net heat flux obtained under real-world weather conditions. Additionally, this research examines various operational scenarios to optimize the receiver's thermal efficiency. Operational safety is also considered through a proposed steam interchange approach to ensure the receiver's reliability and longevity. Ultimately, optimal electricity generation by the turbine-generator system can be achieved by accounting for off-design factors (weather conditions variations), which, to the best of the authors' knowledge, have not been previously addressed.

1.1- Novelty and Contributions

- Multi-Parameter Transient Analysis: Unlike previous research, which relies on average heat flux or unchanged environmental conditions, this work employs a quasi-transient 1-D model integrated with the SolarPILOT tool to account for realistic DNI

variations and actual weather conditions (ambient and sky temperatures) throughout the day.

- Comprehensive Investigation: While the literature focuses on either the north-facing panels or specific receiver sections, this research thoroughly assesses the performance of the evaporator and superheater sections, considering all receiver sides (North, East, South, West).
- Novel Safety Strategy: This study proposes a mass-flow-rate-interchange approach utilizing temperature-control valves to prevent hot spots. This approach encompasses mass flow exchange between opposing superheater receiver sides based on tube wall temperature peaks, offering a simpler alternative to the cross-over designs reported in the literature.

2- MATHEMATICAL MODELING

2.1- Physical Model

The Ivanpah Solar Electric Generation System (ISEGS) CSP Plant is located in California, the United States [30]. This plant has been considered a reference for the current investigation for several reasons. First and foremost, it is based on an external solar collector formed of multiple rectangular-shaped receivers, which represent the key interest of the current piece of research. The second is that it is one of the most recently established plants of its kind worldwide, having been in service since 2014. The hourly-averaged values of DNI adopted in the current analysis have been collected from the weather data provided by the NREL Measurement and Instrumentation Data Center (MIDC) [31]. Meteorological information with high precision is provided by the extensive database of NREL [32], including various locations, whether in the United States or worldwide. 21st June 2015, summer solstice day, has been selected to conduct the current analysis with the DNI readings reported by the closest NREL station to the Ivanpah plant,

i.e., University of Nevada in Las Vegas [31], as listed in **Table 1**. Geographical information of the ISEGS plant is 36.107°N-latitude & 115.1425°W-longitude with an elevation of 615 m AMSL and Universal Time Coordinated of (UTC – 7).

Table 1

The Ivanpah plant consists of three subunits, with a total gross capacity of 392 MW and a net capacity of 377 MW. Those subunits are Ivanpah I, which produces 126 MW, along with Ivanpah II and III, which each produce 133 MW. The heliostats field consists of a total of 173,500 mirrors; 53,500 heliostats are installed on Ivanpah I, in addition to 60,000 in each of Ivanpah II and III, with a 15 m^2 aperture area per heliostat utilized. Each subunit, on the other hand, has an identical tower height of 140 m. As all three subunits forming the ISEGS plant share the same design and operational conditions, except that Ivanpah II and III have slightly larger heliostat fields, only Ivanpah I has been considered for the current analysis. It features a rectangular-shaped solar external receiver composed of three sections: evaporator, superheater, and reheater, as illustrated in **Fig. 2** [33]. The receiver has an overall height of 23.8 m with a square base measuring 16 m on each side. Each section of the receiver consists of 32 panels, each measuring 2 m in width. Details of the HTF tubes forming the panels of the three receiver sections can be found in **Table 2** [33]. It is worth noting that this research focuses on examining the

thermal performance of the evaporator and superheater sections under real-world climate conditions. The reheater section, on the other hand, is not analyzed here as it repeats the operational procedure of the evaporator and superheater sections. Subsequently, the HTF leaving the evaporator section can be in the form of subcooled water, unsaturated steam, or superheated steam, depending on the solar irradiation intensity during the day.

Fig. 2

Table 2

2.2- Assumptions

To reduce the complexity of the under-consideration problem while maintaining a great extent of realism, the assumptions below are followed:

1- Instantaneous value of the DNI incident over all heliostats' subfields is identical.
2- The HTF is evenly distributed over the receiver's four sides.
3- Owing to the similarity in flow configuration among absorbing tubes in each section of the receiver, a single HTF tube from each side has only been considered for the thermodynamic analysis of the receiver sections.
4- The wall thermal resistance of the tube is insignificant and can be ignored.
5- To reduce the size of the current problem, an axisymmetric approximation has been adopted, which requires a uniform heat flux applied to the entire perimeter of the HTF tube. However, the rear half of the tube is thermally insulated, while the front half is

unevenly heated, as shown in **Fig. 3**. This assumption reduces the computational complexity of a 3D or 2D non-symmetric problem to that of a transient 1D analysis. This approach relies on the principle of energy conservation; hence, the total solar power Q_T intercepted by the front of the tube, accounting for the tube's curvature and the incident angle of the solar beam, is considered. This total power is then redistributed as an 'effective' uniform heat flux ($q_w|_{Axisymmetric}$) over the entire tube perimeter. This ensures that the total thermal energy entering the fluid remains physically accurate while allowing for a significantly more efficient numerical solution that still captures the dominant axial and temporal variations. This approach has been validated in [26] as providing a high degree of realism for predicting bulk fluid properties and average wall temperatures.

6- Following assumptions (4 & 5), the transport phenomena involved can be considered one-dimensional, disregarding any variations in the radial direction. Therefore, only bulk changes along the axial direction of the tube have been considered.

7- The heat gain process involved can be assumed quasi-transient, meaning that only transient influences due to temporal variation in solar heat gain have been considered.

8- According to a former scale analysis [26], natural convection to the ambient of the receiver dominates and overwhelms the role played by forced convection. So, heat losses due to forced convection can be neglected.

9- Depending on the HTF phase, its thermophysical characteristics, excluding the specific heat, are all considered constant with values referenced to the onset temperature of each state.

Fig. 3

2.3- Governing Equations and Boundary Conditions

Conservation principles of mass and energy form the backbone of the current thermodynamic analysis, considering the time dependence and axisymmetric approximation of the problem currently under investigation. So, conservation of thermal energy can be applied to the boundaries of an HTF tube control, as follows:

$$\frac{dH_{HTF}}{dt} = \sum_w Q \rightarrow \frac{\Delta H_j}{\Delta t} = Q_{w,net_j} \quad (1)$$

For heating the HTF sensibly, the energy conservation equation is simply written as:

$$\dot{m}\, cp\, \Delta T_{b_j} = q_{net_j} A_{s,out} \quad (2.a)$$

While for the latent form of heating, it is:

$$\dot{m}\, LH_{fg}\, \Delta x_j = q_{net_j} A_{s,out} \quad (2.b)$$

where Δx_j represents the increase in steam vapor fraction generated within a certain element of the tube in the y-direction.

As the outer surface of the HTF tube is subjected to a time-dependent concentrated solar heat flux (q_w) reflected by the heliostats field, a fraction of this heat is lost to the surrounding ambient due to convection and radiation heat transfer. Thus, the net rate of heat flux (q_{net}) gained by the tube wall is evaluated as follows:

$$q_{net} = q_w - q_{conv} - q_{rad} \quad (3)$$

where q_{conv} and q_{rad} are the convective and radiative thermal losses to the ambient.

Depending on the HTF state at any discrete section of the tube, up to three different heating phases can be pronounced throughout the daytime. First, a subcooled region is

established, where liquid water experiences sensible heating. Then, latent heating dominates once solar irradiance becomes strong enough to start water evaporation. As the solar heat gain continues to increase, wet steam is completely converted into superheated steam, and sensible heating prevails, establishing a purely superheated region in the remaining part of the tube. Hence, for predicting the sensible heating processes, the equations below can be employed:

$$Re_i = \frac{4\dot{m}}{\pi d \mu_i} \tag{4}$$

$$h_i = 0.023 \frac{k_i}{d} Re_i^{0.8} Pr_i^{1/3} \tag{5}$$

where (i) stands for the water state at the start of the subcooled or superheated region. Note that eq (5) is valid as the flow is assumed to be fully developed turbulent in a smooth-surface circular tube, $Re \geq 10000$, and $L/D > 10$. In the current analysis, the flow is turbulent in the subcooled and superheated regions, hence Re is 26150 and 283880, respectively.

$$\dot{m} cp(T_{ex} - T_{in}) = q_{net} A_{s,out} \tag{6}$$

$$T_b = \frac{T_{in} + T_{ex}}{2} \tag{7}$$

$$h_i A_{s,in}(T_w - T_b) = q_{net} A_{s,out} \tag{8}$$

Progress in the evaporation process can be, on the other hand, tracked in terms of the increase realized in the water vapor generated per unit length of the tube as follows:

$$\dot{m}\, LH_{fg} \Delta x = q_{net}(\pi D \Delta y) \tag{9}$$

Integrating over a particular section of the tube gives:

$$x = \frac{\pi D\, q_{net}}{\dot{m}\, LH_{fg}}\, y \tag{10}$$

As the objective of the pre-developed mathematical model was to conduct an accurate but simplified enough thermodynamic analysis, the model established by Kandlikar [34] to predict the two-phase flow heat transfer coefficient of saturated steam flow in copper or stainless steel tubes has been adopted due to its compatibility with a variety of heat transfer fluids, including water. Note that this model has an uncertainty of 15.9% compared to the water data. Also, model accuracy may shrink at high vapor qualities. However, it can effectively characterize the dependence of the boiling heat transfer coefficient (h_{TP}) upon the mass flux (G), net wall heat flux (q_{net}), and vapor fraction (x) as follows [34]:

$$h_{TP} = \max(h_{cbd}, h_{nbd}) \tag{11}$$

Where the convective-boiling dominant (h_{cbd}) and nucleate-boiling dominant (h_{nbd}) heat transfer coefficients can be evaluated as follows [34]:

$$h_{cbd} = (1-x)^{\frac{4}{5}} h_l [1.136\, CO^{-0.9} + 667.2\, BOLG^{0.7}\, F] \tag{12.a}$$

$$h_{nbd} = (1-x)^{\frac{4}{5}} h_l [0.6683\, CO^{-0.2} + 1058\, BOLG^{0.7}\, F] \tag{12.b}$$

where F is a surface-fluid combination factor equal to 1 for water [34], while the convection (CO) and boiling ($BOLG$) numbers are defined as follows:

$$CO = \left(\frac{1-x}{x}\right)^{\frac{4}{5}} \left(\frac{\rho_v}{\rho_l}\right)^{\frac{1}{2}} \tag{12.c}$$

$$BOLG = \frac{q_{net}}{LH_{fg}\, G} \tag{12.d}$$

Then,

$$h_{TP} A_{s,in} (T_w - T_{sat}) = q_{net} A_{s,out} \tag{13}$$

The above-detailed mathematical model can be closed using two boundary conditions. The first is the hydrothermal conditions at the evaporator inlet, where a $(105\ kg/s)$ total mass flow rate of $(160\ bar)$ pressurized water flows into it with a bulk temperature of $(460\ K)$. The other one is the thermal condition on the outer surface of the tube wall, which is subjected to a transient field of concentrated heat flux (q_w). Nevertheless, only a fraction of the received flux participates in the heating process due to thermal losses to the ambient by convection and radiation, which can be calculated as:

$$q_{conv} = h_{out}(T_w - T_{amb}) \tag{14}$$

$$q_{rad} = \sigma\varepsilon\left({T_w}^4 - {T_{sky}}^4\right) \tag{15}$$

It is worth stating that such thermal loss modes not only change in time but also vary locally due to the increased levels of wall temperature (T_w) along the HTF tube. Temporal development of the relevant weather data, i.e., ambient temperature (T_{amb}), have been first collected [31] for the diurnal period selected and then correlated as [26]:

$$T_{amb}(K) = 305.65 - 1.448 \times 10^{-5}t + 9.09 \times 10^{-8}t^2 - 5.564 \times 10^{-12}t^3 + 1.82 \times 10^{-16}t^4 - 2.86 \times 10^{-21}t^5 + 1.693 \times 10^{-27}t^6 \tag{16}$$

On the other hand, the transient variation of sky temperature $\left(T_{sky}\right)$ can be approximated as follows [35]:

$$T_{sky}(K) = 0.0522\left(T_{amb}(K)\right)^{3/2} \tag{17}$$

whereas emissivity (ε) of the tube outer surface is taken as $(\varepsilon = 0.86)$ [36].

Finally, heat losses due to convective heat exchange between the tube outer surface and the ambient have been attributed solely to natural convection. This consideration is based on a former scale analysis [26] conducted to quantify the significance of each

convective component relative to the other, which indicates that free convection overwhelms the role played by forced convection, i.e., $O(Ri)\sim 10^5 \gg 1$. Thus, the heat transfer coefficient over the outer surface of the tube has been estimated following the model developed by Al-Arabi and Khamis [37] for free convection over slender cylinders that are oriented vertically:

$$h_{out} = 0.47 \frac{k_{air}}{L} \frac{(Gr_L Pr)^{1/3}}{(Gr_D)^{1/12}} \quad (18)$$

Note that the applicability of Eq. (18) is limited to vertical slender cylinders only ($\theta = 0$).

2.4- Approximation of Heat Flux Distribution for Axisymmetric Analysis

As mentioned earlier, the Ivanpah I rectangular receiver consists of three sections, each comprising four sides, and each side consists of eight panels. Those panels are formed by multiple tubes attached to each other and exposed to high-intensity solar irradiation. Another aspect that should be considered is the transient phenomena resulting from the temporal fluctuations in solar irradiance during daytime. Therefore, taking all tubes and transient issues into account is quite difficult and computationally costly. To cope with such challenges, given the similarity among tubes, one absorbing tube is simulated on each side of the evaporator and superheater, as stated in the assumption. That simplification would substantially decrease the solution grid size, resulting in significant savings in simulation time and computational cost. To this end, the average thermal flux (q_r) is computed by dividing the total solar power on each incident receiver side by its total area at certain times. Note that only the front half of the receiver tubes intercepts the concentrated solar flux. Moreover, such incident heat flux has an irradiance beam component that is not completely effective over the entire tube wall

[38]. This is due to the tube wall curvature in the circumferential direction, which causes the dissipation of solar beams tangent to its outer diameter, as shown in **Fig. 4** [26]. Therefore, to adhere to the concept of energy conservation, careful attention must be paid to this issue to ensure that the solar flux distribution is accurate. Following a modified Gaussian distribution analysis, the normal solar beam component (q_w) on the tube surface is calculated as shown in **Fig. 4**, as follows [39]:

$$q_w = q_n = q_r \sin\theta, \quad (0 \le \theta \le \pi) \tag{19}$$

Then, the total solar power applied to the tube surface (Q_T) can be calculated as [38]:

$$Q_T = \int_{A_s} q_w dA = \left|\int_0^{\pi} q_w r_0 d\theta\right| = q_r r_0 \left|\int_0^{\pi} \sin\theta d\theta\right| = 2 q_r r_0 \tag{20}$$

One practical approach to reducing the problem size and handling thermodynamic or CFD analyses of SPT solar receivers involving transport phenomena is to employ an axisymmetric approximation. That requires applying a uniform heat load to the entire circumference of the absorbing tube. However, the rear side of the absorbing tube is insulated, whereas the front side is not uniformly heated due to the aforementioned reasons. So, to implement such an approximation to a higher limit of reality, the total solar power applied to the tube wall, i.e. $Q_T = 2 q_r r_o$ as Eq.(20) states, is divided by the tube perimeter, as demonstrated in **Fig. 3**, to make sure that only the effective component of solar thermal power is utilized uniformly over the tube perimeter, as follows [26]:

$$q_w|_{Axisymmetric} = \frac{Q_T}{2\pi\, r_o} = \frac{q_r}{\pi} \tag{21}$$

Fig. 4

3- SIMULATION PROCEDURE

3.1- SolarPILOT Simulation

The commercial software "SolarPILOT" established by NREL [28], which is based on the Monte Carlo ray tracing technique [40], is used to precisely detect heat flux maps on the solar receiver tubes. The procedure of simulation using the SolarPILOT tool has been detailed in our earlier work [26], considering the assumptions stated there. After establishing the actual land boundaries of the Ivanpah I plant in CA, USA, as illustrated in **Fig. 5**, the plant design characteristics are specified, including the realistic optical height achieved by implementing the Radial Stagger layout for the heliostats' solar field, which minimizes shading effects. Such effects occurring between neighboring heliostats inhibit reflected irradiance from reaching the receiver-absorbing tubes [26]. Then, the heliostats' optical properties are also configured, including their geometry, focus parameters, optical error parameters, and mirror performance parameters. After that, the receiver geometry, receiver position, optical properties, and the design thermal losses are established. Accordingly, the temporal profile of incident wall heat flux, shown in **Fig. 6**, is computed first [26]. Then, it is converted to an axisymmetric heat flux "equivalent to the real-world heat flux applied" for each side of the receiver using Eq.(21). Note that thermal losses because of convection and radiation are presented as virtual zero values to implement the current simulation. Nevertheless, such losses are precisely computed in the developed in-house MATLAB code [26]. It is worth mentioning that such profiles are useful not only in quasi-transient one-dimensional thermodynamic analysis but also for two-dimensional CFD simulations.

Fig. 5

Fig. 6

3.2- Numerical Solution

A MATLAB code has been developed to numerically solve the current 1-D and transient problems. Then, a discretization scheme has been applied to the entire physical domain (evaporator and superheater tubes). Hence, the physical domain is divided into multiple cylindrically shaped longitudinal segments, as demonstrated in **Fig. 7**. After that, temporal fluctuations in meteorological data have been calculated using relevant correlations. Then, at every time step, an iterative solution is performed to accurately predict the HTF bulk temperature and the tube wall temperature. Consequently, the net heat flux gained, depending on the thermodynamic state of the HTF, is automatically corrected for each single control volume of the domain. Such an iterative solution has been conducted individually on each side of the evaporator. Once the overall steam produced in this section of the receiver is harvested, it undergoes one of three operational scenarios before being fed to the superheater section. Scenario #1 involves combining the productivity of the evaporator's four sides, feeding the mixture directly, and distributing it evenly to each superheater section side. Such a Scenario was used to operate the old-fashioned SPT facilities. Scenario #2, on the other hand, involves delivering steam vapor only to the superheater section by further heating the evaporator output using auxiliary boilers during off-peak periods. This Scenario has been adopted as the standard operational procedure for the Ivanpah I plant since 2014. It is worth noting that Scenarios #1 and #2 experienced operational issues, including the formation of hot

spots due to overheating, particularly in the superheater section. This is why Scenario#3 has been proposed and evaluated for its potential to address the overheating problem while maintaining the targeted productivity. Hence, Scenario #3 is similar to the second one but utilizes the excess thermal energy of the superheated steam during the peak period to compensate for some of the energy required to fully evaporate the steam during the off-peak times. The convergence criterion is the maximum change in the tube wall temperature across iterations, with a quantitative limit of 10^{-6}. It is a dimensionless criterion computed as follows:

$$Err. = \mathrm{ABS}\left(T_{W_{new}} - T_{W_{prev.}}\right)/T_{W_{prev.}}$$

The numerical solution independence from the grid size adopted in the current analysis has, on the other hand, been verified for six grid sizes with increments of y equal to 0.1, 0.05, 0.01, 0.005, 0.001, and 0.0005 m, as **Table 3** demonstrates. Results revealed that the changes in the calculated data were negligible between the fifth and sixth mesh sizes, i.e. 0.006%. Therefore, an element size of $1mm$ is selected in the current analysis. Consequently, as the heat flux gain processes are presumably quasi-transient, only the transient effect as a result of temporal fluctuations in solar thermal gain is considered. Namely, the accuracy of the numerical scheme is not affected by the size of the timestep. Thus, a timestep size of $\Delta t = 5min$ is selected to provide results with high temporal resolution.

Fig. 7

Table 3

4- RESULTS

4.1- Thermal Response to Instantaneous Meteorological Conditions Variation

To explore the thermal response of the Ivanpah I receiver to the time-changing weather conditions over daytime under the Scenario #1 of operation, the temporal and local change of net heat flux received by each side of the evaporator, as well as the superheater section, has first been illustrated in **Fig. 8**. It is observed that the net heat flux obtained by each side of the evaporator section is, in general, higher than the corresponding one in the superheater section. This is attributed to the continuous increase in tube wall temperature as the steam passes from the evaporator to the superheater section, as shown in **Fig. 9**. This, in turn, increases overall losses due to convection and radiation from the superheater section, slightly reducing the net heat gained there compared to the evaporator section. However, such losses in the evaporator and superheater are highly sensitive to time and location on the tube due to their direct dependence on the tube's surface temperature. This linkage is illustrated in **Fig. 10** based on the temporal and local distribution of bulk temperatures along each side of the evaporator and superheater. As the solar thermal flux varies during the daytime, the tube wall temperature responds accordingly, resulting in variations in heat losses and the HTF bulk temperature. Nevertheless, once HTF reaches the saturation limit, the phase-change phenomenon plays a substantial role in alleviating the tube wall temperature level and holding a certain margin of temperature excess, i.e. $\Delta T_{excess} = T_w - T_{sat}$, leading to a reduction in heat losses. One can clearly identify the evaporation zone by observing the vapor fraction produced temporally and locally, as demonstrated in **Fig. 11**. In the

subcooled zone, where no steam has yet been generated, HTF receives thermal power in the sensible mechanism. Once the evaporation process begins, the inner convective heat transfer coefficient rapidly increases, accompanied by a gradual rise in the HTF vapor produced. When the evaporation process is complete, i.e., x equals 1, the HTF is further heated sensibly to become superheated steam, as indicated by the heat transfer patterns and steam produced in the superheater section. It is worth mentioning that all the patterns discussed above are for Scenario #1 operation case, where, regardless of the state of steam generated within the evaporator, it is passed directly to the superheated section and distributed evenly over its four sides.

Fig. 8

Fig. 9

Fig. 10

Fig. 11

Once the overall steam produced in this section of the receiver is harvested, it undergoes one of three scenarios before being fed to the superheater section. To gain a better understanding of the thermal performance of the receiver, the temporal profiles of steam bulk temperature, productivity rate, and specific enthalpy are plotted at the outlet of each side of the evaporator and superheater, as shown in **Figs. 12, 13,** and **14**, respectively. It is worth noting that the above-mentioned figures are relevant to Scenario #1 of the operation, where the productivity of each side of the evaporator is combined before feeding the resulting mixture directly into the superheater, ensuring an even distribution to each side. The impact of dissimilarity in concentrated solar irradiance

applied on each side of the receiver is obvious from the divergence between the temporal evolution of steam bulk temperature, particularly along the evaporator and to a lesser extent in the superheater section, as shown in **Fig. 12**. To further explain the solar irradiance dissimilarity, in the morning, the angle between the solar irradiance incident and the reflected irradiance is quite large for the heliostats in the eastern field, whereas it is considerably smaller for the heliostats on the western side. Note that the smaller angle produces greater solar flux on the corresponding side of the receiver. However, this scenario is overturned in the afternoon as the western heliostats deliver less concentrated solar power than the eastern ones due to the larger angle of incident irradiance. Therefore, during the early morning, the west side of the evaporator experiences a faster rise in steam thermal content because it is exposed to higher solar intensity than the other sides, as shown in **Fig. 6**. A similar observation can be made regarding the development of steam temperature along the east side, which is pulsed up during the afternoon, whereas on either the north or south side, it reaches its peak at midday. Furthermore, such developments in heat content along each side of the receiver are subdivided into three distinct areas, depending on the state of the steam generated, namely subcooled heating, boiling, and superheating, which evolve at different rates depending on the temporal solar intensity to which they are exposed. Accordingly, the temporal rate of the vapor produced by each side of the evaporator and superheater will differ as well, as **Fig. 13** reveals. One would observe that the low steam generation rate in the early morning is attributed to the poor contribution of the eastern side of the evaporator and the superheater. Likewise, in the late afternoon, the west side of either

the evaporator or superheater makes a poor contribution to steam generation due to the low solar irradiance during these two periods of the day. Accordingly, as the west side of the evaporator or superheater starts producing steam earlier than the other sides, the east one continues producing steam later in the day due to the dissimilarity explained in the solar heat flux. The overall rate of vapor produced by the evaporator, on the other hand, resembles the temporal DNI profile used to generate the concentrated solar power. However, this is not the case in the superheater section, where the steam profile generated there is flattened over most of the daytime hours.

From an operational perspective, the specific enthalpy represents the heat content required to operate the steam turbine and generate electric power. Therefore, as **Fig. 14** depicts, the overall specific enthalpy exiting the evaporator meets the superheater inlet operational condition, i.e. $x = 1$, with some excess in steam energy for the period extending from 8:15 to 16:10, even though the state of steam at the outlet of some sides of the evaporator may not necessarily fulfill that condition. This is attributed to the excess in energy, over $h_v = 2.581\ MJ/kg$, allowing other sides to contribute to the mixing process at the evaporator outlet, thereby compensating for this thermal energy shortage. Knowing that the specific enthalpy of steam required to meet the turbine inlet condition is nearly $h_{TIC} = 3.426\ MJ/kg$. On the other hand, the superheater section can extend the plant's stand-alone operation to more than 9 hours (7:10 to 16:25).

Fig. 12

Fig. 13

Fig. 14

536
537 **4.2- Sensitivity of Plant Productivity to Weather Conditions and Operation Scenarios**

538 In common with Scenario #1, both Scenario #2 and #3 involve the same patterns in
539 the evaporator section. The difference, however, is that only steam is to be delivered to
540 the superheater section by further heating the evaporator output using auxiliary boilers
541 during off-peak periods. Therefore, only characteristics of the steam produced by the
542 superheater will be further discussed and compared for the operation scenarios tested.
543 Scenario #2 is based on delivering steam only into the superheater section, but without
544 shaving any excess energy the evaporator produces during peak time. To explore the
545 impact of adopting such an operational scenario, the outlet bulk temperature of the
546 steam produced by the superheater versus day hours is illustrated in **Fig. 15**. As the steam
547 fed into the superheater is entirely in a vapor state, it continues to receive sensible heat,
548 allowing it to reach higher temperatures. The maximum temperature of the overall steam
549 generated at midday is around 835 K, enough to meet the SST-900 steam turbine inlet
550 temperature requirement (818 K); hence, such a turbine is employed in the Ivanpah plant
551 to generate electricity [41]. However, additional thermal energy must be provided to
552 cover the shortage in thermal energy during the early morning and late afternoon periods,
553 as well as to meet the enthalpy requirement necessary to operate the turbine throughout
554 the day. The outlet-specific enthalpy profile in **Fig. 15** demonstrates that Scenario #2 is
555 capable of covering the steam enthalpy requirement of the turbine, i.e., $3.426\ MJ/kg$,
556 for 9 hours from 07:20 to 16:20. Scenario #3 is, on the other hand, quite similar to the
557 latter one but with a subtle difference. It exploits the excess thermal energy in the
558 superheated steam produced by the evaporator during peak times to compensate for

559 some of the energy required to fully evaporate the wet steam generated during off-peak
560 periods, as shown in **Fig. 16**.

561 **Fig. 15**

562 **Fig. 16**

563 To better highlight the difference in performance between the three operational
564 scenarios, the overall bulk temperature and specific enthalpy of the steam delivered by
565 the superheater are illustrated in **Fig. 17**. Overall, Scenarios #2 and #3 outperform
566 Scenario #1 in extending the period during which the solar receiver can nearly fulfill the
567 turbine steam inlet conditions required. However, that comes at an implicit extra cost due
568 to the need for a backup fossil-fuel boiler to make up the thermal energy required for
569 feeding only vapor steam into the superheater section. Therefore, it is better to examine
570 the makeup required closely and the excess power available by the end of both the
571 evaporator and superheater sections under any of the operation scenarios tested.

572 **Fig. 17**

573 The turbine used is the SST-700/900 by Siemens, which has an inlet steam
574 temperature range from 380 to 550°C [41]. However, the optimal steam inlet
575 temperature for operation analysis is 545°C [33], corresponding to the steam specific
576 enthalpy of 3.426 MJ/kg at an operating pressure of 16 MPa. This threshold specifies the
577 turbine operating conditions that must be fulfilled for reliable operation over daytime
578 periods. So, if the steam produced by the evaporator or superheater has a specific
579 enthalpy above 2.581 or 3.426 MJ/kg, respectively, excess energy will be instantaneously
580 available there as follows:

$$Q_{Excess}|_{Evap.} = \dot{m}_t(h - h_v) \quad (22.a)$$

$$Q_{Excess}|_{Sup.} = \dot{m}_t(h - h_{TIC}) \quad (22.b)$$

While the makeup required, if any, is the amount of instantaneous power below the above-mentioned conditions, as follows:

$$Q_{Makeup}\big|_{Evap.} = \dot{m}_t(h_v - h) \quad (23.a)$$

$$Q_{Makeup}\big|_{Sup.} = \dot{m}_t(h_{TIC} - h) \quad (23.b)$$

Fig. 18 compares the receiver's overall performance under all three operational scenarios examined. It is apparent that the total makeup energy required for all scenarios tested is almost the same. However, the difference lies in the mechanism for exploiting any excess power available. For the first and second operation scenarios, excess power in the evaporator is not harvested, unlike Scenario #3, which has lower thermal content steam fed into the superheater due to the shaving of excess power produced by the evaporator section. This implies, as **Fig. 19** indicates, that the second scenario is expected to produce higher power excess by the end of the superheater section than the last one. However, this is not the case, as Scenario #3 appears to be producing a higher excess in power. This is attributed to higher thermal losses during Scenario #2 due to the higher wall temperatures expected, resulting from the higher thermal content of steam fed into the superheater section. This implicit difference may positively impact the receiver's daily productivity compared to both other scenarios. To verify this, the overall receiver productivity under any of the examined operation scenarios has been evaluated in terms of the makeup, excess, and net energy required to ensure reliable turbine operation throughout the entire day, as shown in **Table 4**. Accordingly, it is confirmed that Scenario

#3 outperforms in terms of net productivity due to the lower overall makeup required throughout the day. Under which, the receiver can meet 93.61% of the plant steam demand when operating standalone, compared to 90.44% and 89.06% when Scenarios #1 and #2 are, respectively, adopted for operation. In other words, the comparative analysis shows that Scenario #3 reduces the total net makeup energy required by approximately 33% compared to Scenario #1 and 41.5% compared to Scenario #2.

Fig. 18

Fig. 19

Table 4

4.3- Operation Safety and Reliability

At this stage, a question may arise about the feasibility of increasing the number of heliostats to harvest more solar power, and consequently, increasing the rate of electric power produced by the plant under consideration. Though such a proposal may sound appealing initially, it may entail two serious consequences. The first arises from an economic perspective, driven by increased capital costs. The second, from a safe-operation point of view, is due to the potential for generating extremely concentrated heat flux and its impact on the durability of the receiver structure. The maximum allowable temperature for the receiver tubes should be specified first to explore the latter aspect. Bearing in mind that the long lifetime of the receiver would be affected by the long-lasting extreme levels of tube wall temperature while in operation, time-dependent deformation of the tube material is expected to evolve. Multiple failure cases due to high temperature can be attributed to either creep or a combination of creep and fatigue,

where the temperature regime, in Kelvin, for which creep is important in metals, is $\left(0.5T_{melting} < T < T_{melting}\right)$ [42]. Note that the evaporator and superheater panels are formed from tubes made from stainless-steel alloys not publicly published, which have a roughly 1450℃ melting point. Therefore, the tube wall temperature limit can be considered $\left(TWTL = 0.5T_{melting} = 861.575K\right)$ [42]. It is worth noting that operational safety is specifically checked for Scenario #3 of the operation, as it has outperformed the other two.

Inspecting the change in tube wall temperature over the daytime reveals that the maximum wall temperatures on each side of the receiver are detected at different times of the day, depending on the temporal heating intensity to which they are exposed. Such levels are respectively reached on the west, north, south, and east sides of the receiver at 9:35, 13:05, 14:20, and 14:45, as shown in **Fig. 20**, which demonstrates the local distribution of tube wall temperature on each side of the evaporator and superheater sections. Accordingly, it is observed that only the ends of the tubes on the evaporator's north side experience such extreme conditions and may face the hazard of creep. On the other hand, the situation is more severe on the superheater panels, where up to 30% of the length of the tubes on either the north or east side might undergo creep issues due to exceeding the maximum allowable wall temperatures. However, only 6% of the tubes forming the west side may face such issues, with the south panels experiencing no such problems.

Fig. 20

To sum up, hotspots, if allowed, are likely to generate in specific locations of the receiver panels. This is why certain precautions must be implemented to reduce the negative impact of such unavoidable issues. One of the strategies followed is to defocus the heliostat field to reduce the concentration level of the solar field. However, this means reducing the amount of solar energy harvested, downgrading the receiver's instantaneous steam productivity. Another proposal is to bypass the molten salt HTF between the opposing receiver tubes, which are exposed to different levels of solar intensity. To do so, the panels located on opposite sides of the receiver are interconnected in a cross-over manner [29]. However, this remedy is hard to implement and may complicate the receiver design. To overcome this latter complication, a new mass flow rate interchange approach is proposed to control the steam inlet mass flow rate to each side of the superheater based on the maximum wall temperature detected. Three mass flow interchange processes have been employed to address this issue. The first is from the south to the north panels during the peak solar irradiance on the north face, the second is from the west to the east panels at the peak solar irradiance on the east side, while the last one is from the east to the west panels during the peak solar irradiance on the west side. With the aid of a temperature control valve (TCV), a fraction of the mass flow rate, which is allocated to a certain side of the superheater (CF) is redirected to flow through the opposing side's tubes once hot spots emerge over their surfaces. So, three circulation factors ($CF_{E\rightarrow W}$, $CF_{S\rightarrow N}$, and $CF_{W\rightarrow E}$), referring to the percentage of water that is circulated between the two opposing panels mentioned above, have been adopted as key factors for optimized performance, as follows:

$$T_{N\max} \geq TWTL \rightarrow \begin{Bmatrix} \dot{m}_N = (1 + CF_{S\rightarrow N})\,\dot{m}_t/4 \\ \dot{m}_S = (1 - CF_{S\rightarrow N})\,\dot{m}_t/4 \end{Bmatrix} \quad (24.a)$$

$$T_{E\max} \geq TWTL \rightarrow \begin{Bmatrix} \dot{m}_E = (1 + CF_{W\rightarrow E})\,\dot{m}_t/4 \\ \dot{m}_W = (1 - CF_{W\rightarrow E})\,\dot{m}_t/4 \end{Bmatrix} \quad (24.b)$$

$$T_{W\max} \geq TWTL \rightarrow \begin{Bmatrix} \dot{m}_W = (1 + CF_{E\rightarrow W})\,\dot{m}_t/4 \\ \dot{m}_E = (1 - CF_{E\rightarrow W})\,\dot{m}_t/4 \end{Bmatrix} \quad (24.c)$$

Thus, different wall responses and thermal performance patterns are expected based on the amount of mass flow circulated. So, an optimization analysis has been conducted to check the impact of the circulation factor (CF) adopted for mass interchange between each pair of the opposing sides listed in Eq.(24). For seeking brevity, the next discussion is dedicated to only presenting the results relevant to the optimum values of the circulation factor. Several circulation factors are considered to guarantee that the superheater tube wall temperatures do not exceed $TWTL$, which is $0.5T_{melting}$. For the south-to-north circulation ($CF_{S\rightarrow N}$), it is observed that 0.25 prevents the tube wall temperature from reaching the critical limit, as shown in **Fig. 21**. From a thermodynamic point of view, reducing the steam mass flow rate to the south side does not necessarily imply a decrease in overall thermal gain, as the north panel experiences an increase in thermal gain. On the other hand, the optimal circulation factor between the east and west panels ($CF_{W\rightarrow E}$, and $CF_{E\rightarrow W}$) at the maximum solar irradiance is 0.1375 for both panels, as shown in **Fig. 22**. To further clarify that, in the first half of the day, the west side experiences higher solar irradiance. Thus, the direction of steam interchange is from east to west to cool the tube wall. The steam mass flow in the east panel was carefully monitored to avoid exceeding the east tube wall temperature limit. In the second half of the day, however, the east side of the receiver receives high levels of concentrated solar

radiation. Therefore, the direction of mass interchange is from west to east. By adopting such a mass interchange, the temperature levels of the tubes exposed to extreme thermal input can be alleviated, as shown in **Fig. 21 and Fig. 22**. However, as the wall temperatures on the extremely heated sides are lowered, the corresponding opposing sides experience a rise in such levels due to the reduced steam flow inside; hence, less heat can be carried away from their tube walls. The latter outcome is practically significant as the sides that participate in a fraction of their flow rate experience a rise in the level of their specific enthalpy produced, such that the overall steam power generated by the receiver is unaffected.

Fig. 21

Fig. 22

Such an observation can be better highlighted by comparing the specific steam enthalpy generated by the superheater with and without utilizing a TCV, as shown in **Fig. 23**. It is interesting to note that the current proposal for TCV utilization to manage the temperature levels of receiver tubes does not result in any reduction in the overall thermal energy harvested by the steam produced. In other words, an uneven distribution of steam fed into the superheater sides guarantees the receiver's safety and maintains the plant's reliability by delivering the same output as before. As shown in **Table 5**, proposing an uneven distribution not only reduces the total makeup energy required but also slightly improves the excess available, resulting in a saving of about 0.75% of the energy needed to fulfill the turbine inlet condition. Hence, it reduces the receiver's net makeup ratio by about 0.626%.

Fig. 23

Table 5

5- CONCLUSIONS

Solar power plants have great potential to generate electricity through solar thermal power, which naturally fluctuates spatially and temporally. Therefore, this research presents a comprehensive transient thermal analysis of the performance of a solar power tower receiver under realistic weather conditions. The Ivanpah I plant is selected as the reference plant, and the simulation covers the entire day of June 21st, 2015. The SolarPILOT tool simulates the heliostat field configuration and the transient heat distribution across the solar receiver panels. The effective component (perpendicular) of concentrated solar power is estimated following a modified Gaussian distribution over the tube circumference. A MATLAB code was successfully developed to evaluate key thermal parameters, including net heat flux, steam heat content, tube wall temperature, and vapor fraction, for both the evaporator and superheater sections. Three operational scenarios have been examined and compared based on the state of the steam entering the superheater section. The optimization reveals that, among the operational scenarios tested, the receiver under Scenario #3 outperforms in terms of net productivity and efficiency, meeting 93.61% of the overall plant steam demand. Nevertheless, localized overheating in the superheater tubes has been identified as a safety concern. To mitigate this, a mass flow redistribution approach with optimal circulation factors between the opposing sides is proposed using a temperature control valve. It was found that an uneven distribution of steam fed into the superheater sides can achieve a 0.75%

reduction in the energy required to meet the turbine inlet condition, with a 0.626% decrease in the net makeup ratio of the receiver. In brief, the proposed approach demonstrates strong potential to optimize receiver thermal performance and ensure safer, more efficient operation of solar thermal power plants.

6- Future Scope

- Extending the transient simulation to describe the startup and shutdown operation, considering the thermal stresses throughout the diurnal cycle.
- Detecting the hot spots on the receiver tube wall in advance to enable the designers of such plants to apply specific control/operation strategies to avoid thermal stresses and mechanical failure.
- Exploring plant efficiency employing advanced HTFs, such as supercritical carbon dioxide (CO_2) and particle-based systems.

FUNDING

This research received no specific grant from any funding agency in the public, commercial, or not-for-profit sectors.

NOMENCLATURE

A	Area, m^2
BOLG	Boiling number
CF	Circulation factor
CO	Convective number
cp	Specific heat, J/kg· K
D	Outer diameter, m
d	Inner diameter, m

G	Mass flux, kg/m^2·s
Gr	Grashof number
g	Gravitational acceleration, m/s^2
h	Specific enthalpy, J/kg; convective heat transfer coefficient, W/m^2·K
k	Thermal conductivity, W/m· K
F	Fluid-solid combination factor
L	Tube length, m
L_{fg}	Latent heat of vaporization, J/kg
$\dot{m}$	Mass flow rate, kg/s
Pr	Prandtl number
$\dot{Q}_{inc}$	Total incident thermal power on the receiver surface, W
Q_T	Concentrated solar power incident on the receiver, W
q	Heat flux, W/m^2
$q_{Axisymmetric}$	Axisymmetric heat flux, W/m^2
Re	Reynolds number
Ri	Richardson number
T	Temperature, K
t	Time, s
U	Velocity, m/s

x	Vapor fraction
y	Distance in y-direction, m

Greek Symbols

β	Volume expansion coefficient, 1/K
ρ	Density, kg/m^3
μ	Dynamic viscosity, Pa. s
v	Kinematic viscosity, m^2/s
ε	Tube outer emissivity
σ	Stefan-Boltzmann constant, W/m^2·K^4
α	Receiver surface reflectivity

Abbreviations

CSP	Concentrating solar power
DNI	Direct normal irradiance
DSG	Direct steam generation
HTF	Heat transfer fluid
ISEGS	Ivanpah Solar Electric Generating System
NREL	National Renewable Energy Laboratory
TWTL	Tube wall temperature limit
TCV	Temperature control valve

752 **Subscripts**

amb	Ambient
b	Bulk
cbd	Convection boiling dominant
conv	Convection
D	Along the tube diameter
ex	Exit section
E	East side
in	Inlet section, inner tube surface
i	Subcooled or superheated section
j	Location index
L	Along the tube length
N	North side
n	Normal
net	Net
nbd	Nucleate boiling dominant
out	Outer tube surface
r	Average
rad	Radiation

S	South side
s	Surface
sat	Saturation
sky	Sky
t	Tangential, total
TP	Two-phase
v	Vapor
W	West side
w	Wall

753

REFERENCES

[1] Alhusseny, A., Al-Zurfi, N., Al-Aabidy, Q., Nasser, A., and Al-Madhhachi, H., 2024, "Response to the Design Conditions of a Tube-Bundle Thermal Energy Storage Unit with Paraffin-Copper Foam Composite as a Storage Medium," Int. J. Heat Mass Transf., **228**(April), pp. 1–17. https://doi.org/10.1016/j.ijheatmasstransfer.2024.125679.

[2] Gupta, P. K., 1999, "Renewable Energy Sources-a Longway to Go in India," Renew. Energy, **16**, pp. 1216–1219. https://doi.org/10.1016/S0960-1481(98)00486-8.

[3] Abbott, D., 2010, "Keeping the Energy Debate Clean: How Do We Supply the World's Energy Veeds?," Proc. IEEE, **98**(1), pp. 42–66. https://doi.org/10.1109/JPROC.2009.2035160.

[4] Tian, Y., and Zhao, C. Y., 2013, "A Review of Solar Collectors and Thermal Energy Storage in Solar Thermal Applications," Appl. Energy, **104**, pp. 538–553. https://doi.org/10.1016/j.apenergy.2012.11.051.

[5] Dascomb, J., 2009, "Low-Cost Concentrating Solar Collector for Steam Generation," M.Sc. thesis, Florida State University, Florida, USA.

[6] Mukesh, B. S., Mukhopadhyay, S., Mondal, A., and Chandra, L., 2022, "Numerical Design and Studies of Multipurpose Concentrated Solar Thermal Heating System," ASME J Therm Sci Eng Appl, **14**(7), pp. 1–13. https://doi.org/10.1115/1.4053017.

[7] Elmorsy, L., Hamdy, S., Morosuk, T., and Tsatsaronis, G., 2022, "Evaluating the Market Potential of Concentrated Solar Thermal Technology for Different Applications in the MENA Region," ASME J Energy Res Technol, **144**(5), pp. 1–13.

776 https://doi.org/10.1115/1.4051744.

777 [8] Fang, L., Li, Y., Yang, X., and Yang, Z., 2020, “Analyses of Thermal Performance of
778 Solar Power Tower Station Based on a Supercritical CO2 Brayton Cycle,” ASME J
779 Energy Res Technol, **142**(3), pp. 1–7. https://doi.org/10.1115/1.4045083.

780 [9] Colakoglu, M., and Durmayaz, A., 2022, “Multiobjective Optimization of a Novel
781 Solar Tower-Based Gas Plant With Energy, Exergy, Economic, and Environmental
782 Impact Analysis,” ASME J Energy Res Technol, **144**(May), pp. 1–14.
783 https://doi.org/10.1115/1.4051805.

784 [10] Plant, C., 2019, “Performance Analysis of Integrated Solar Tower With a
785 Conventional Heat and Power,” ASME J Energy Res Technol, **141**(February), pp. 1–
786 13. https://doi.org/10.1115/1.4041409.

787 [11] Kalogirou, S. A., 2013, “Solar Thermoelectric Power Generation in Cyprus:
788 Selection of the Best System,” Renew. Energy, **49**, pp. 278–281.
789 https://doi.org/10.1016/j.renene.2012.01.014.

790 [12] Weissert, J., Zhou, Y., You, D., and Metghalchi, H., 2022, “Current Advancement of
791 Heliostats,” ASME J Energy Res Technol, **144**(12).
792 https://doi.org/10.1115/1.4054738.

793 [13] Behar, O., Khellaf, A., and Mohammedi, K., 2013, “A Review of Studies on Central
794 Receiver Solar Thermal Power Plants,” Renew. Sustain. Energy Rev., **23**, pp. 12–
795 39. https://doi.org/10.1016/j.rser.2013.02.017.

796 [14] Manente, G., Rech, S., and Lazzaretto, A., 2016, “Optimum Choice and Placement
797 of Concentrating Solar Power Technologies in Integrated Solar Combined Cycle

Systems," Renew. Energy, **96**, pp. 172–189. https://doi.org/10.1016/j.renene.2016.04.066.

[15] Shouman, E. R., and Khattab, N. M., 2015, "Future Economic of Concentrating Solar Power (CSP) for Electricity Generation in Egypt," Renew. Sustain. Energy Rev., **41**, pp. 1119–1127. https://doi.org/10.1016/j.rser.2014.08.067.

[16] Qaisrani, M. A., Fang, J., Jin, Y., Wan, Z., Tu, N., Khalid, M., Rahman, M. U., and Wei, J., 2019, "Thermal Losses Evaluation of an External Rectangular Receiver in a Windy Environment," Sol. Energy, **184**, pp. 281–291. https://doi.org/10.1016/j.solener.2019.03.103.

[17] Fang, J., Qaisrani, M. A., Tu, N., Wei, J., Wan, Z., Jin, Y., Khalid, M., and Ahmed, N., 2022, "Experiment and Numerical Analysis of Thermal Performance of a Billboard External Receiver," Energies, **15**(6), pp. 1–15. https://doi.org/10.3390/en15062188.

[18] Mokhtar, M., Berger, M., Zahler, C., Krüger, D., Schenk, H., and Stieglitz, R., 2015, "Direct Steam Generation for Process Heat Using Fresnel Collectors," Int. J. Therm. Environ. Eng., **10**(1), pp. 3–9. https://doi.org/10.5383/ijtee.10.01.001.

[19] Parzen, M., 2017, "Comparison of Heat Transfer Fluids (HTF) for Solar Tower Systems," University of Applied Sciences Nuremberg, Germany. https://doi.org/10.13140/RG.2.2.23137.15202.

[20] Phelan, P., Otanicar, T., Taylor, R., and Tyagi, H., 2013, "Trends and Opportunities in Direct-Absorption Solar Thermal Collectors," ASME J Therm Sci Eng Appl, **5**(2), pp. 1–9. https://doi.org/10.1115/1.4023930.

[21] Rodríguez-Sánchez, M. R., Soria-Verdugo, A., Almendros-Ibáñez, J. A., Acosta-Iborra, A., and Santana, D., 2014, "Thermal Design Guidelines of Solar Power Towers," Appl. Therm. Eng., **63**(1), pp. 428–438. https://doi.org/10.1016/j.applthermaleng.2013.11.014.

[22] Liu, Y., Wang, W., Zhang, C., Li, T., and Zhao, X., 2024, "Improving the Heat Transfer Performance of the Tower Molten Salt Solar Receiver with the Novel Folded Flow Tubes," ASME J Therm Sci Eng Appl, **16**(2), pp. 1–10. https://doi.org/10.1115/1.4063912.

[23] Crespi, F., Toscani, A., Zani, P., Sánchez, D., and Manzolini, G., 2018, "Effect of Passing Clouds on the Dynamic Performance of a CSP Tower Receiver with Molten Salt Heat Storage," Appl. Energy, **229**(July), pp. 224–235. https://doi.org/10.1016/j.apenergy.2018.07.094.

[24] Cagnoli, M., de la Calle, A., Pye, J., Savoldi, L., and Zanino, R., 2019, "A CFD-Supported Dynamic System-Level Model of a Sodium-Cooled Billboard-Type Receiver for Central Tower CSP Applications," Sol. Energy, **177**(July 2018), pp. 576–594. https://doi.org/10.1016/j.solener.2018.11.031.

[25] Qaisrani, M. A., Wei, J., Fang, J., Jin, Y., Wan, Z., and Khalid, M., 2019, "Heat Losses and Thermal Stresses of an External Cylindrical Water/Steam Solar Tower Receiver," Appl. Therm. Eng., **163**(August), p. 12. https://doi.org/10.1016/j.applthermaleng.2019.114241.

[26] Al-Sarraf, H., Alhusseny, A., and Zamora, R., 2025, "Impact of Weather Conditions Variability on External Receivers in Real-World Direct Steam Generation Solar

Power Tower Plants," ASME J Therm Sci Eng Appl, **17**(September), pp. 1–19. https://doi.org/10.1115/1.4068836.

[27] Sánchez-González, A., Rodríguez-Sánchez, M. R., and Santana, D., 2022, "FluxSPT: Tool for Heliostat Field Aiming and Flux Mapping in Solar Power Tower Plants," Proc. AIP Conf., **2445**, pp. 1–9. https://doi.org/10.1063/5.0085656.

[28] Wagner, M. J., and Wendelin, T., 2018, "SolarPILOT: A Power Tower Solar Field Layout and Characterization Tool," Sol. Energy, **171**(August 2016), pp. 185–196. https://doi.org/10.1016/j.solener.2018.06.063.

[29] Rodriguez-Sanchez, M. R., Sanchez-Gonzalez, A., Marugan-Cruz, C., and Santana, D., 2015, "Flow Patterns of External Solar Receivers," Sol. Energy, **122**, pp. 940–953. https://doi.org/10.1016/j.solener.2015.10.025.

[30] NREL, "Power Tower Projects," Conc. Sol. Power Proj.

[31] NREL, "UNLV Solar Calendars," Meas. Instrum. Data Cent.

[32] NREL, "The National Renewable Energy Laboratory (NREL)."

[33] Plotkin, A. R., Toupin, K. M., Gillum, C. B., Rancatore, R. J., Yang, T., and Mier, D., 2011, "Solar Receiver Steam Generator Design for the Ivanpah Solar Electric Generating System," *Proceedings of the ASME*, Denver, Colorado, USA, pp. 1–7.

[34] Kandlikar, S. G., 1998, "Boiling Heat Transfer with Binary Mixtures: Part II - Flow Boiling in Plain Tubes," Asme J Heat Transf., **120**, pp. 388–394. https://doi.org/10.1115/1.2824262.

[35] Göksu, T. T., 2024, "Energy, Exergy Analysis, and RSM Modeling of Different Designed Twisted Tapes in Placed PV/T Systems," Energy, **304**(June).

https://doi.org/10.1016/j.energy.2024.132041.

[36] Yellowhair, J., Ho, C. K., Ortega, J. D., Christian, J. M., and Andraka, C. E., 2015, "Testing and Optical Modeling of Novel Concentrating Solar Receiver Geometries to Increase Light Trapping and Effective Solar Absorptance," High Low Conc. Syst. Sol. Energy Appl. X, **9559**, pp. 1–11. https://doi.org/10.1117/12.2186647.

[37] Al-Arabi, M., and Khamis, M., 1982, "Natural Convection Heat Transfer from Inclined Cylinders," Int. J. Heat Mass Transf., **25**(I), pp. 3–15. https://doi.org/10.1201/b12772-10.

[38] Boerema, N., Morrison, G., Taylor, R., and Rosengarten, G., 2013, "High Temperature Solar Thermal Central-Receiver Billboard Design," Sol. Energy, **97**, pp. 356–368. https://doi.org/10.1016/j.solener.2013.09.008.

[39] Liao, Z., Li, X., Xu, C., Chang, C., and Wang, Z., 2014, "Allowable Flux Density on a Solar Central Receiver," Renew. Energy, **62**, pp. 747–753. https://doi.org/10.1016/j.renene.2013.08.044.

[40] Mahan, J. R., 2019, *The Monte Carlo Ray-Trace Method in Radiation Heat Transfer and Applied Optics*, John Wiley & Sons Ltd. and ASME Press, USA.

[41] Siemens, 2016, *SST-700/900 Economical Dual-Casing Steam Turbine for Reheat Applications*, Goerlitz, Germany.

[42] Meyers, M. A., and Chawla, K. K., 2009, *Mechanical Behavior of Materials*, Cambridge University Press, Cambridge, UK.

885 **Figure Captions List**
886

Fig. 1 A schematic illustration of the heliostats and solar tower in the SPT plant

Fig. 2 The external rectangular receiver configuration in ISEGS [33]

Fig. 3 Converting a 3-D problem into a 2-D axisymmetric one

Fig. 4 Components of concentrated solar power ($\boldsymbol{q_r}$) on a receiver tube wall

Fig. 5 Aerial image (left) and SolarPILOT heliostats layout simulation (right) of the Ivanpah I plant

Fig.6 Temporal variation of the average heat flux incident on each side of the receiver

Fig. 7 Illustration of the solution element and the boundary conditions surrounding

Fig. 8 Temporal and local variation of net heat flux on the representative tubes of the evaporator (top) and superheater (bottom)

Fig. 9 Temporal and local variation of wall temperature on the representative tubes of the evaporator (top) and superheater (bottom)

Fig. 10 Temporal and local variation of water/steam bulk temperature inside the representative tubes of the evaporator (top) and superheater (bottom)

Fig. 11 Temporal and local variation of steam vapor fraction generated in the representative tubes of the evaporator (top) and superheater (bottom)

Fig. 22 Variation of maximum wall temperature, outlet specific enthalpy, and steam rate for the east (top) and west (bottom) sides of the superheater

Fig. 23 Comparison of the specific enthalpy of steam generated by the superheater with or without utilizing a TCV

887
888

Table Caption List

Table 1: Hourly-averaged DNI readings at the University of Nevada on June 21 (2015) [31]															
Daytime	05:00	06:00	07:00	08:00	09:00	10:00	11:00	12:00	13:00	14:00	15:00	16:00	17:00	18:00	19:00
$I(W/m^2)$	17.1	524.5	749.4	739.7	844.2	887.3	911.9	910.4	956.6	941.3	910.5	834.0	637.3	558.0	193.7

Table 2: Geometrical characteristics of the receiver sections

Receiver section	Tube		Number of panels	Tubes per panel
	Diameter (mm)	Length (m)		
Evaporator	25.4	10.4	32	70
Superheater	19.05	8.5	32	90
Reheater	38.1	4.9	32	46

Table 3: Sensitivity of numerical solution to the size of the element adopted

$\Delta y\ (m)$	0.1	0.05	0.01	0.005	0.001	0.0005
$T_{b,out_{max}}(K)$	643.51799	645.66424	648.35770	648.74097	649.01822	649.05682
$Error\ \%$	---	0.334	0.417	0.059	0.043	0.006

Table 4: Receiver thermal performance under the operational scenarios tested

Operation Scenario	Makeup Energy Required ($MWhr$)			Excess Energy Available ($MWhr$)			Net Required ($MWhr$)	Makeup Percentage
	Evaporator	Superheater	Total	Evaporator	Superheater	Total		
#1	---	515.28	515.28	---	34.85	34.85	480.43	9.54%
#2	441.35	144.56	585.91	---	34.90	34.90	551.00	10.94%
#3	441.35	144.56	585.91	241.11	22.74	236.85	322.05	6.39%

Table 5: Comparison of receiver thermal performance under Scenario#3 without and with TCV

Operation Scenario	Total makeup required ($MWhr$)	Total excess available ($MWhr$)	Net power required ($MWhr$)	Makeup ratio (%)
Without TCV	585.91	263.85	322.05	6.39
With TCV	585.78	266.15	319.63	6.35
Change%	-0.0222	$+0.872$	-0.7514	-0.626

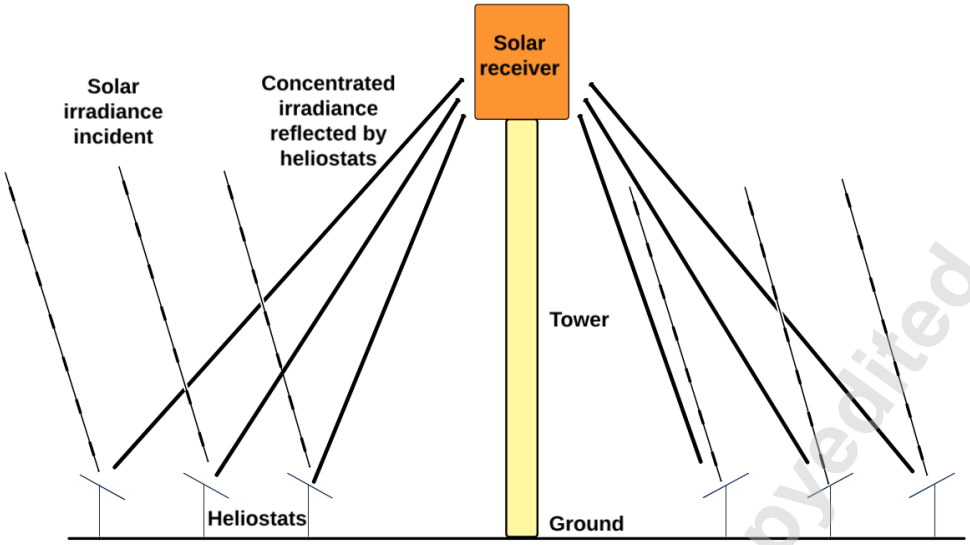

Fig. 1: A schematic illustration of the heliostats and solar tower in the SPT plant

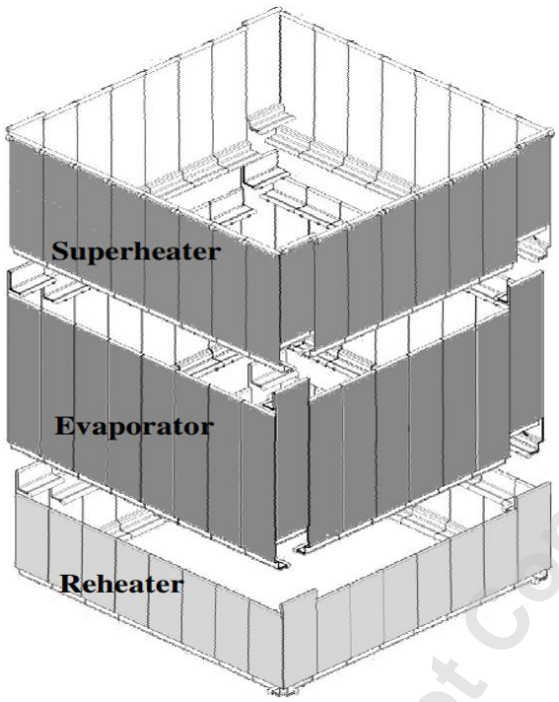

Fig. 2: The external rectangular receiver configuration in ISEGS [33]

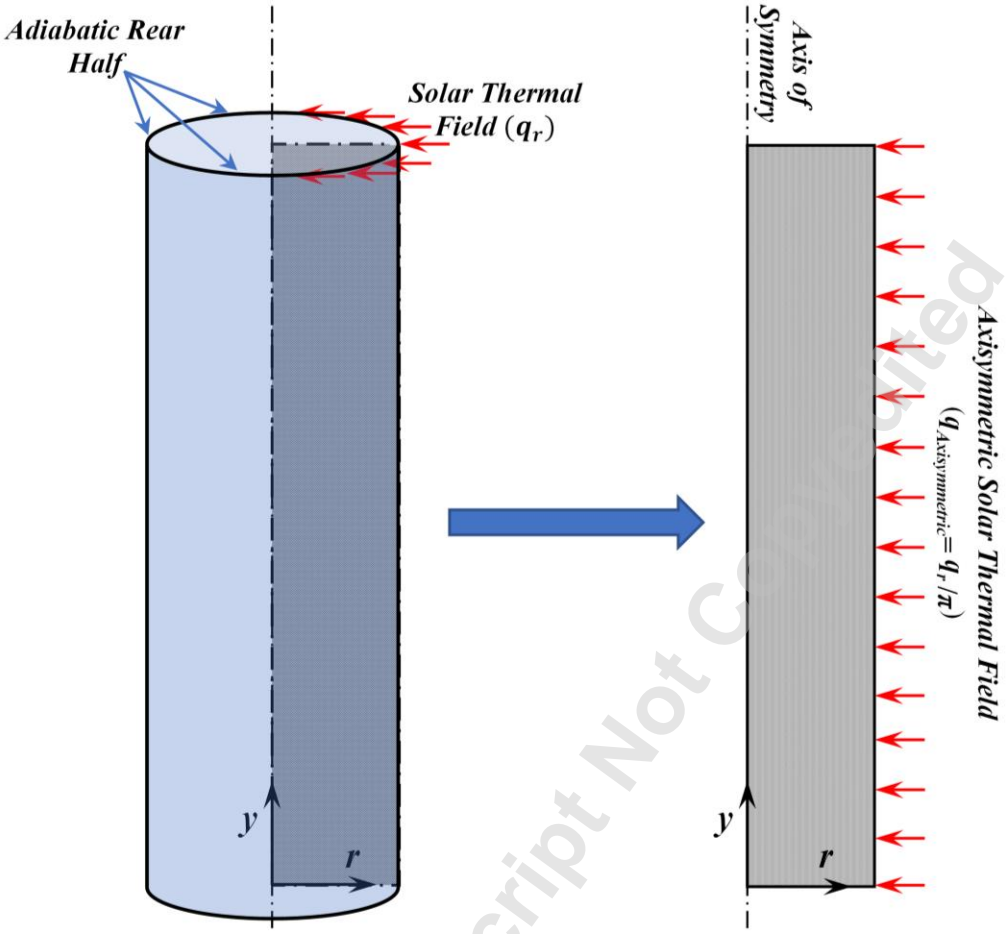

Fig. 3: Converting a 3-D problem into a 2-D axisymmetric one

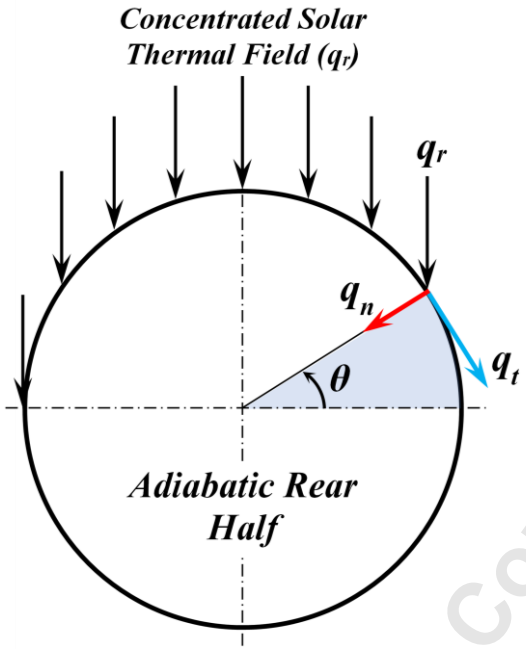

Fig. 4: Components of concentrated solar power (q_r) on a receiver tube wall

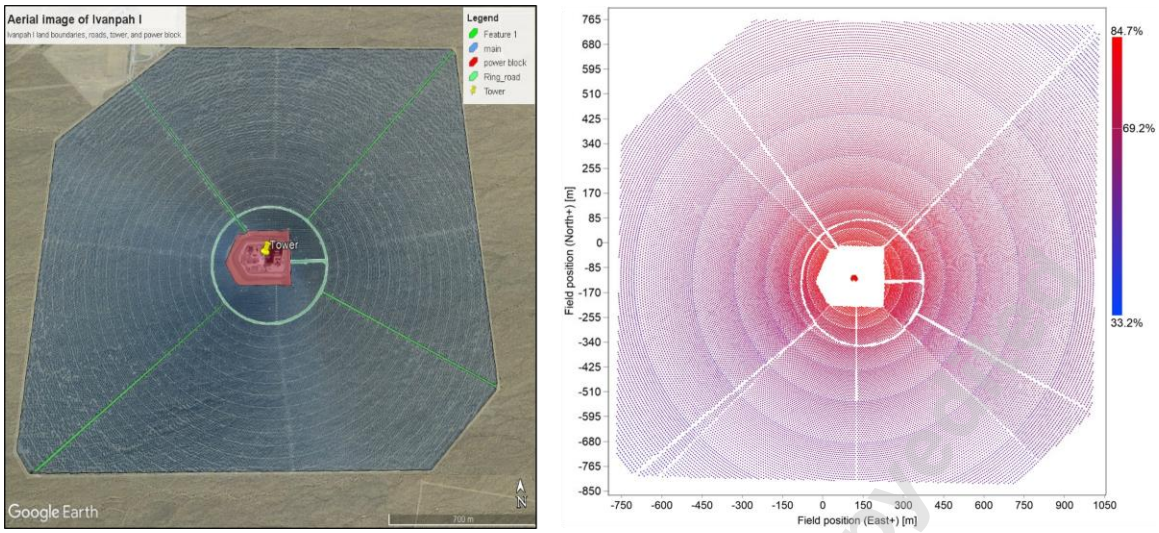

Fig. 5: Aerial image (left) and SolarPILOT heliostats layout simulation (right) of the Ivanpah I plant

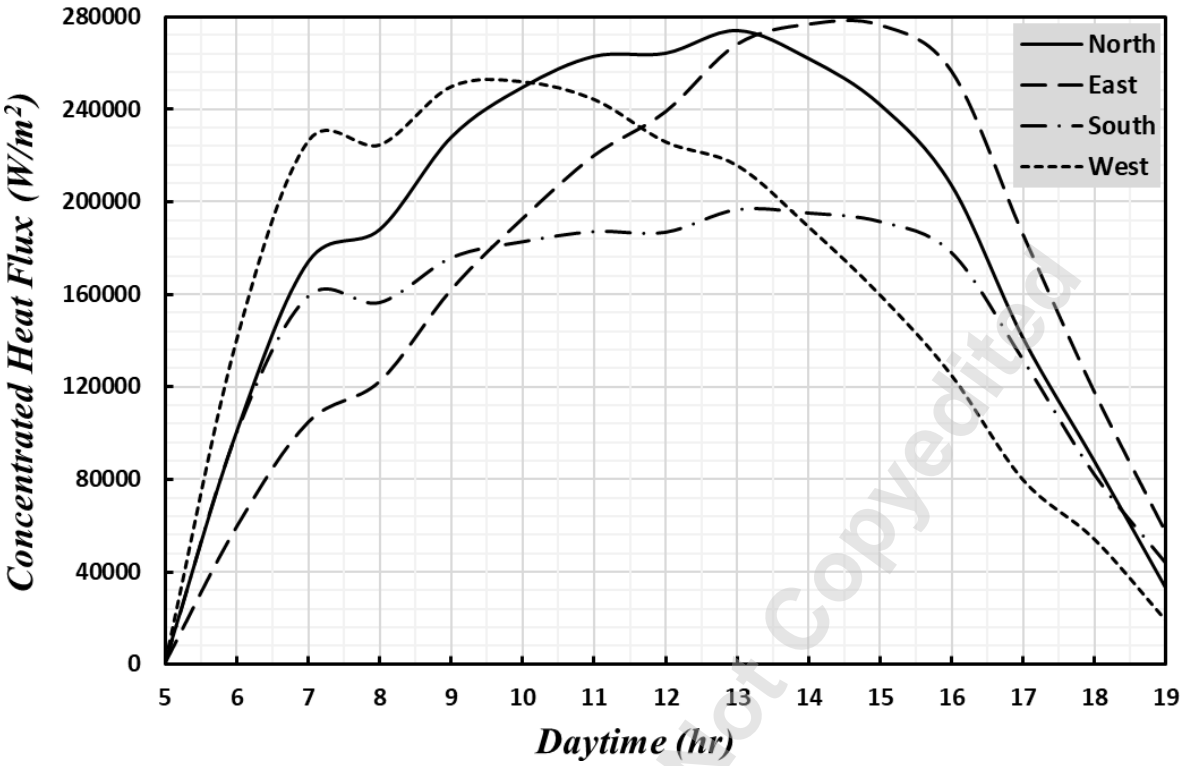

Fig. 6: Temporal variation of the average heat flux incident on each side of the receiver

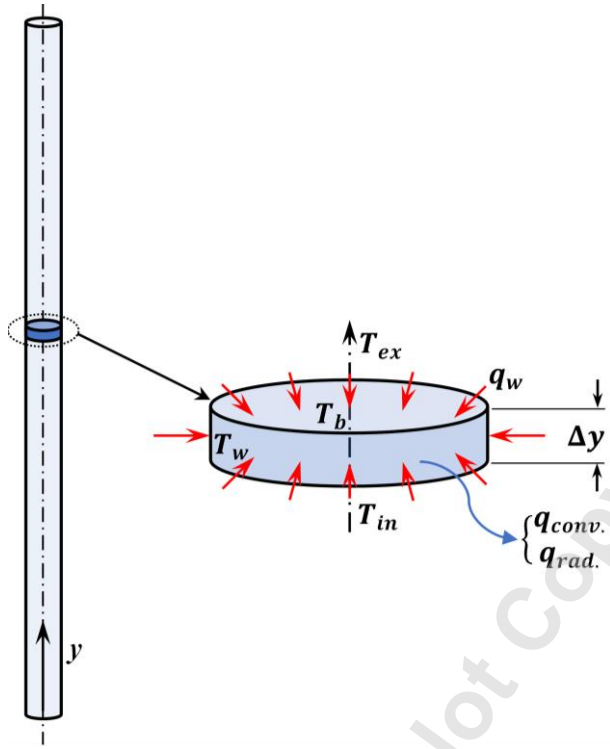

Fig. 7: Illustration of the solution element and the boundary conditions surrounding

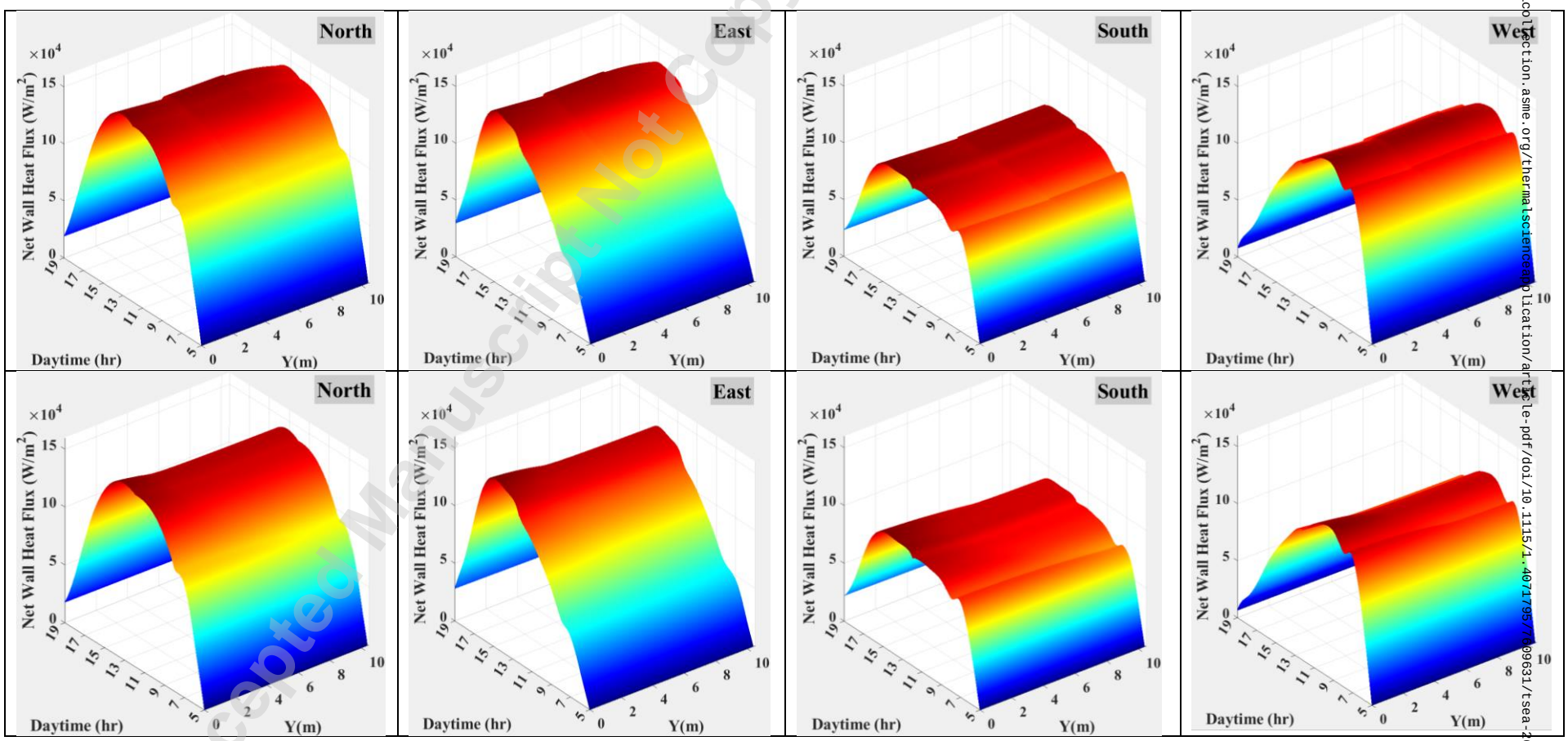

Fig. 8: Temporal and local variation of net heat flux on the representative tubes of the evaporator (top) and superheater (bottom)

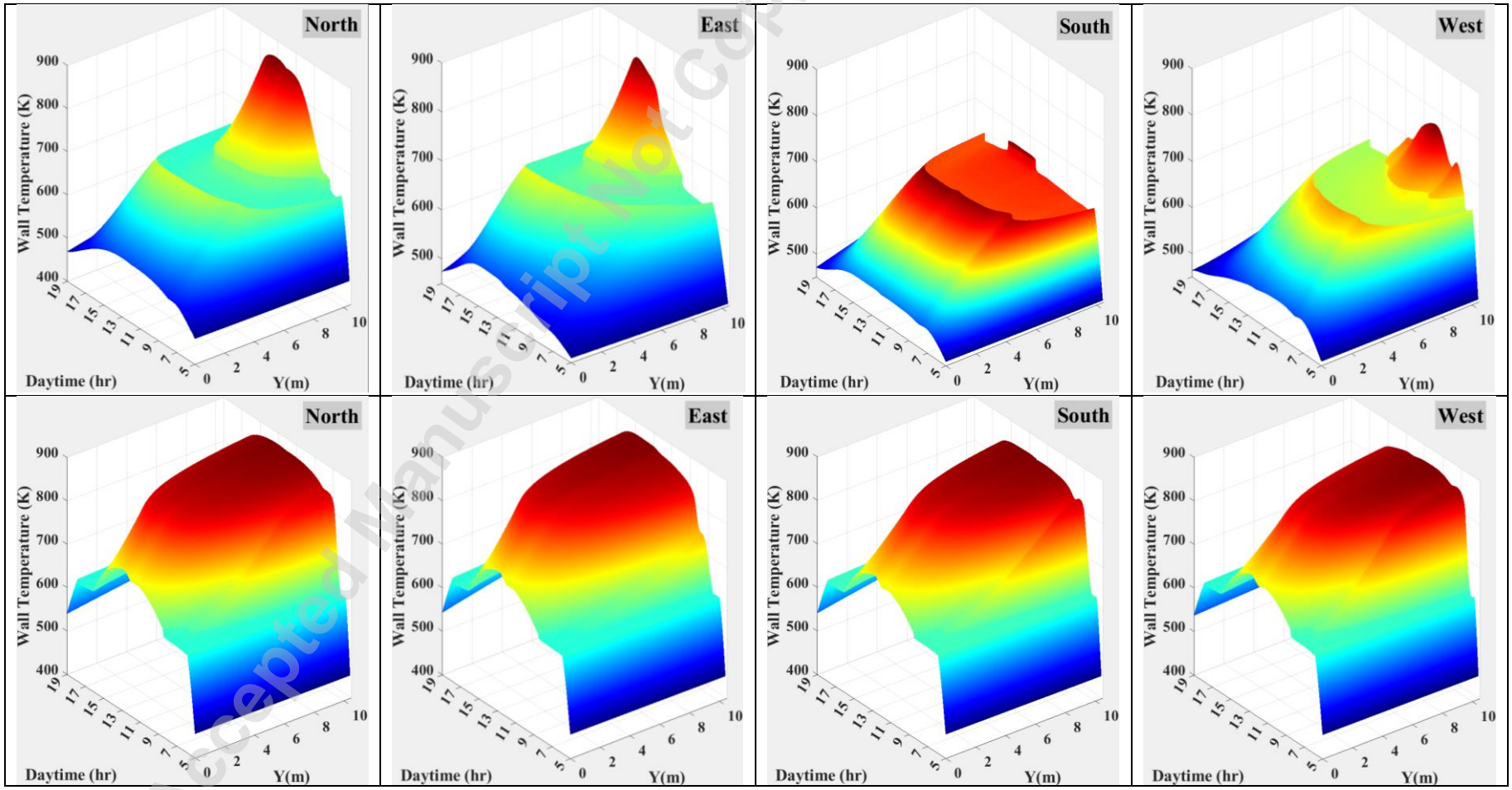

Fig. 9: Temporal and local variation of wall temperature on the representative tubes of the evaporator (top) and superheater (bottom)

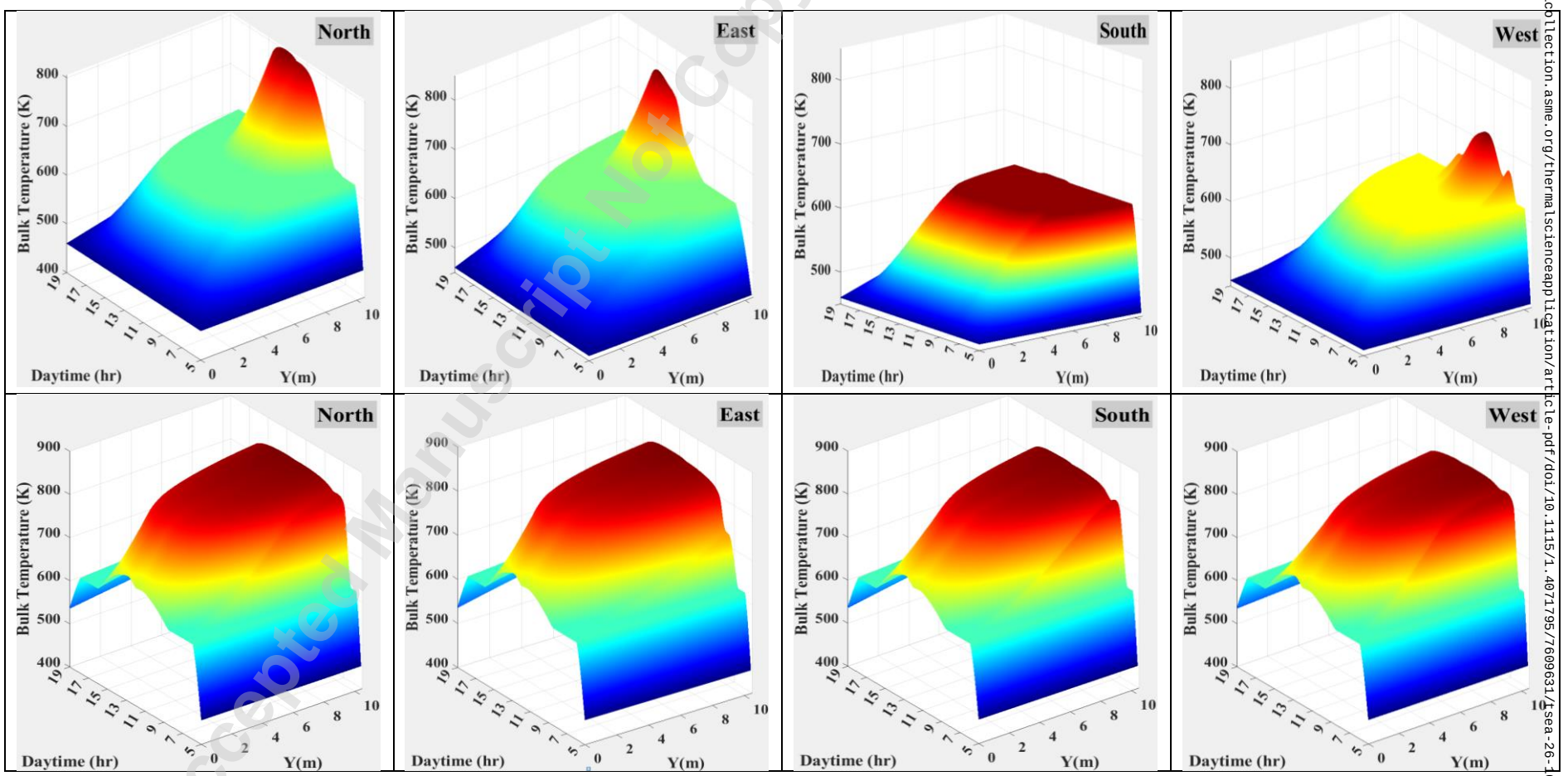

Fig. 10: Temporal and local variation of water/steam bulk temperature inside the representative tubes of the evaporator (top) and superheater (bottom)

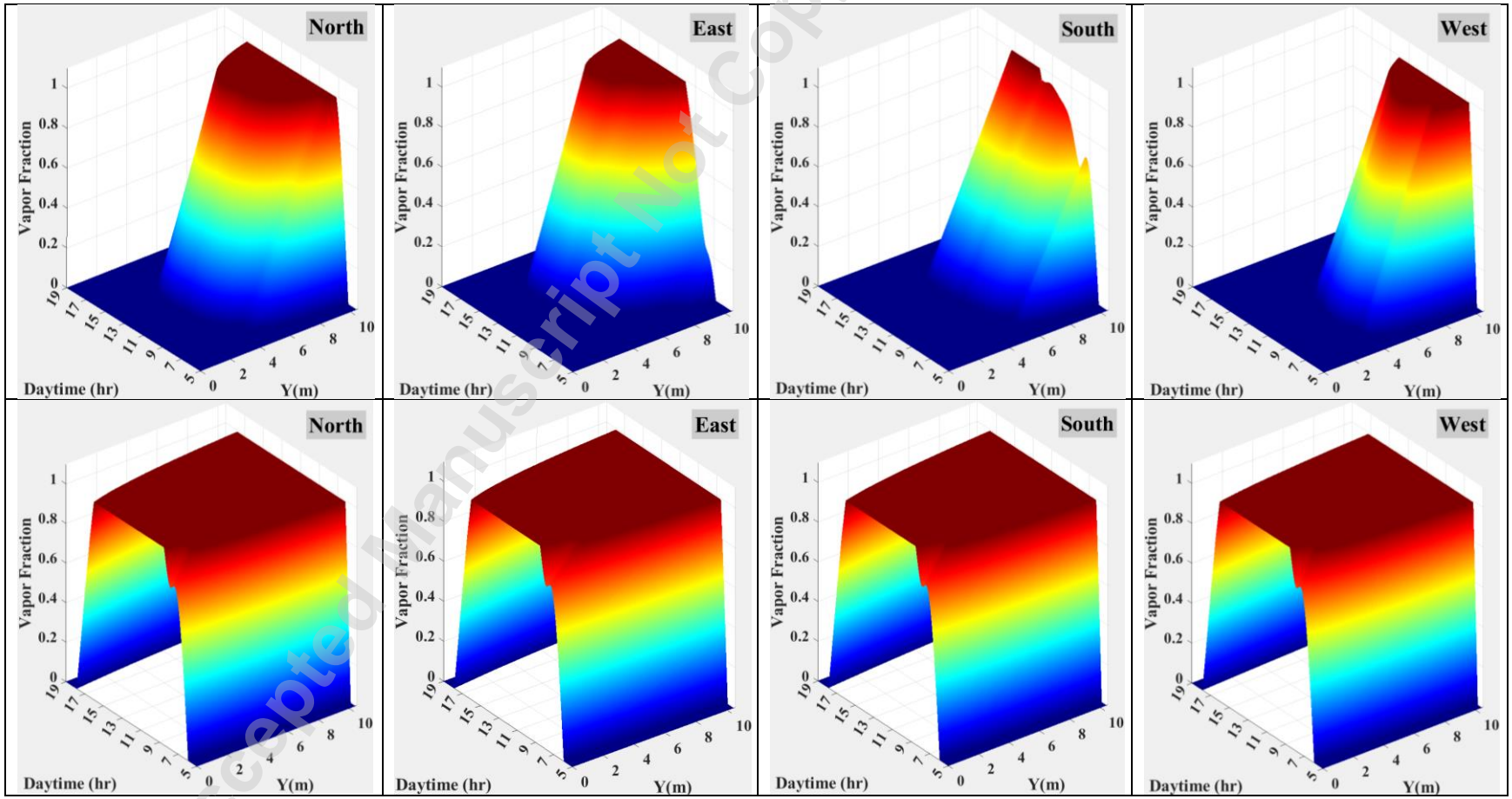

Fig. 11: Temporal and local variation of steam vapor fraction generated in the representative tubes of the evaporator (top) and superheater (bottom)

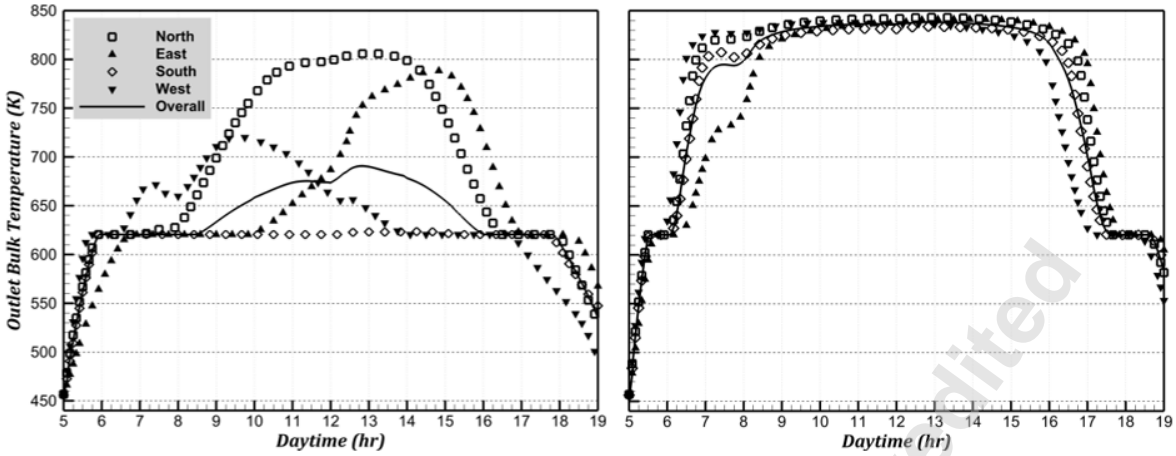

Fig. 12: Scenario #1 profile of outlet bulk temperature on each evaporator side (left) and superheater (right)

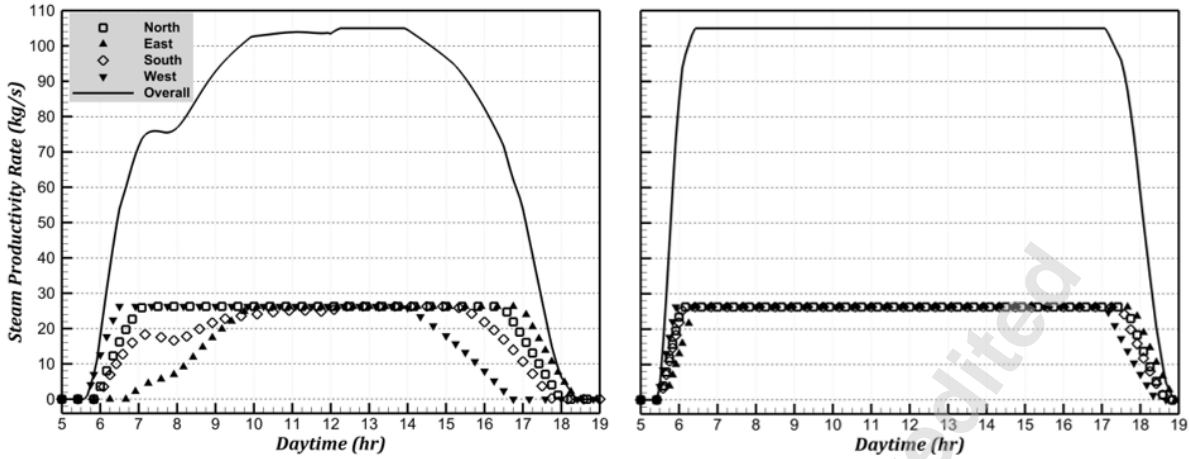

Fig. 13: Scenario #1 profile of steam produced by each side of the evaporator (left) and superheater (right)

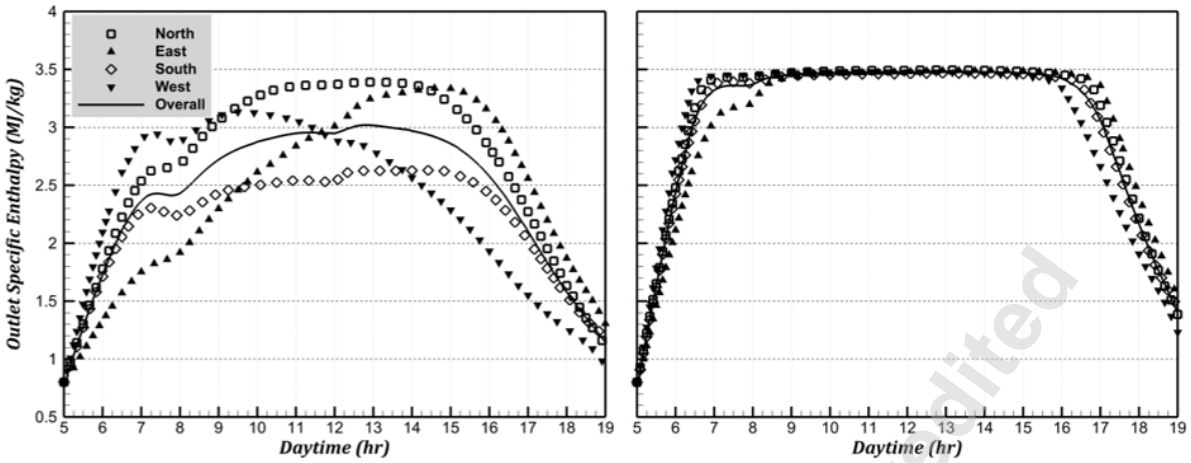

Fig. 14: Scenario #1 profile of steam specific enthalpy on each side of the evaporator (left) and superheater (right)

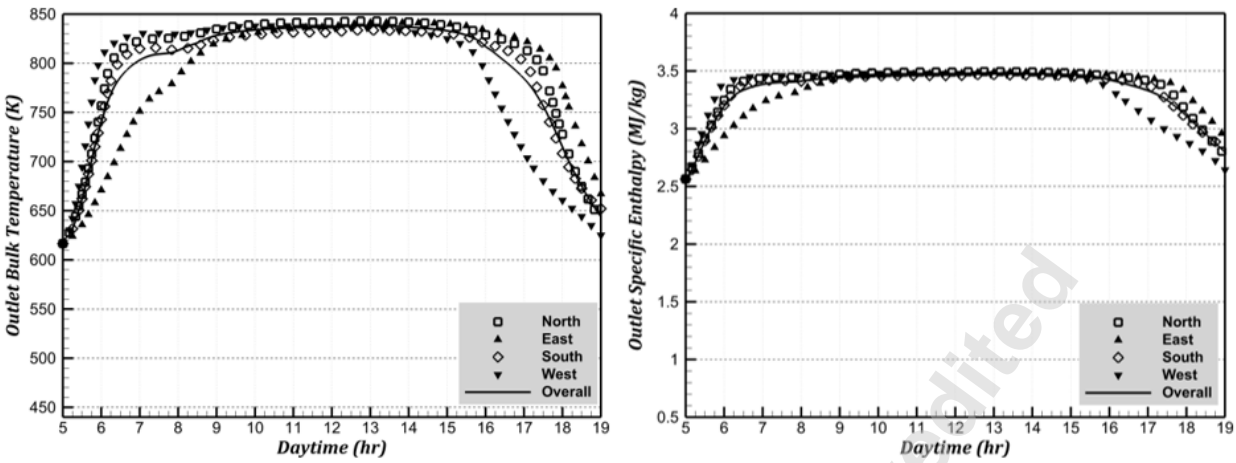

Fig. 15: Scenario #2 profile of bulk temperature (left) and specific enthalpy (right) out of each superheater side

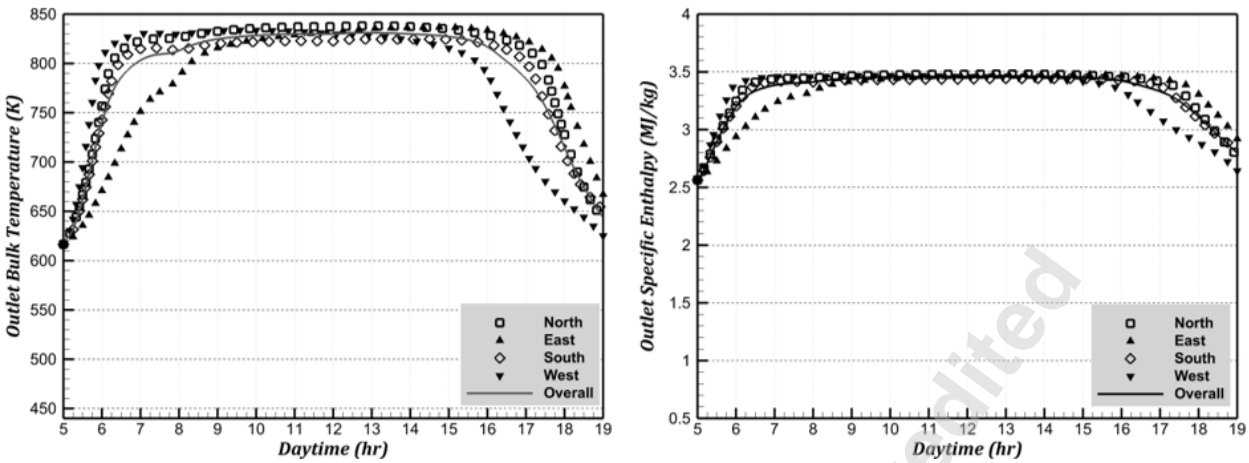

Fig. 16: Scenario #3 profile of bulk temperature (left) and specific enthalpy (right) out of each superheater side

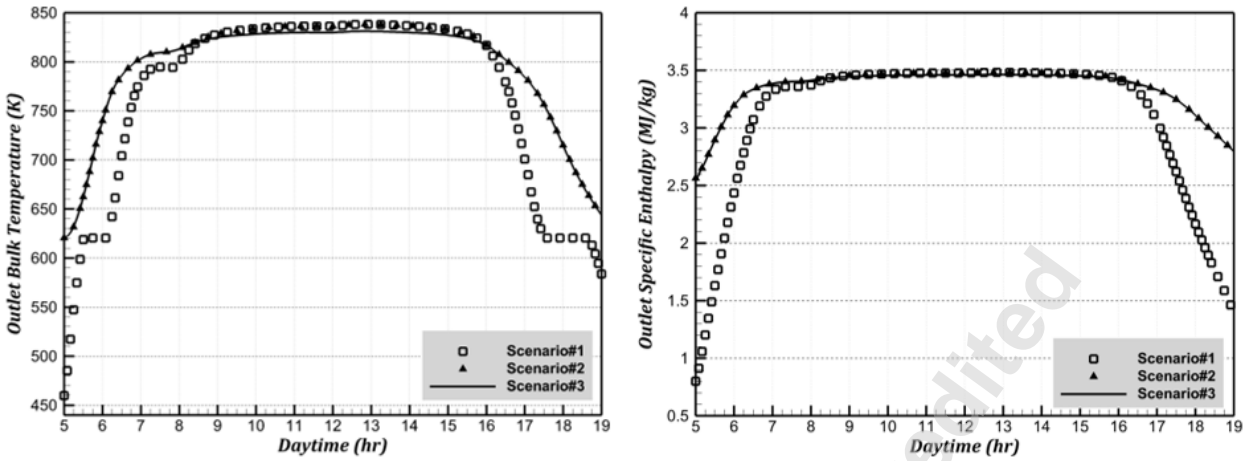

Fig. 17: Comparison of bulk temperature (left) and specific enthalpy (right) for the three operational scenarios

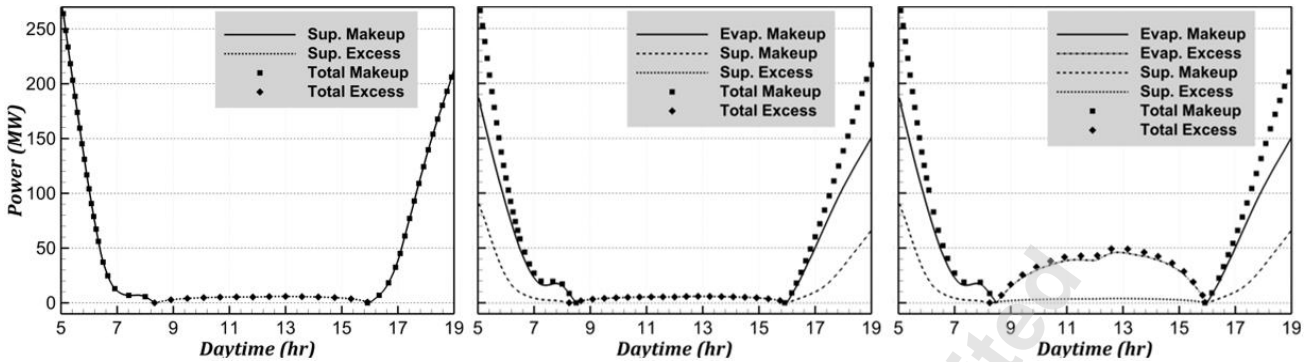

Fig. 18: Profile of the makeup required vs excess power available for (from left to right) Scenario #1, #2, and #3

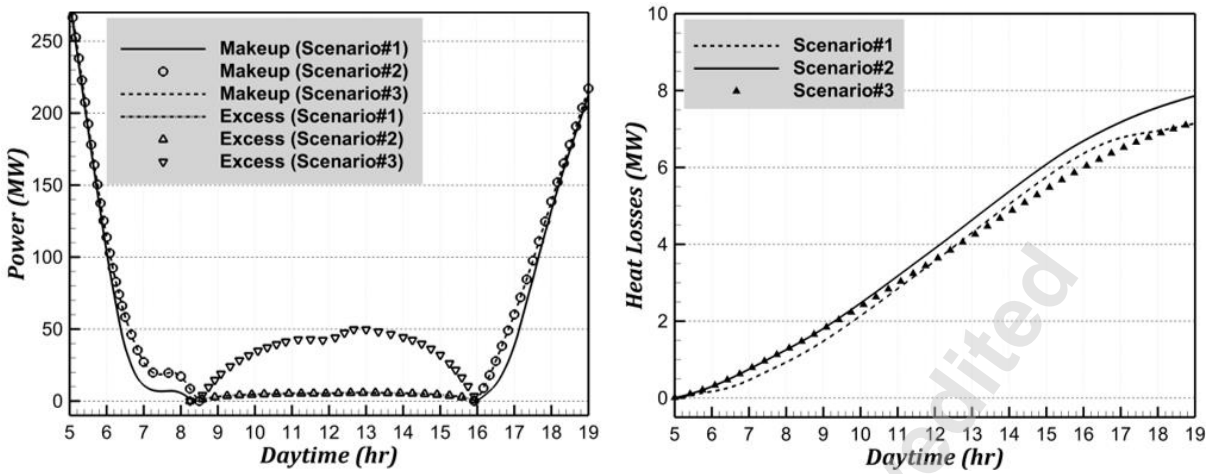

Fig. 19: Total makeup required and excess power available (left) vs superheater heat losses (right)

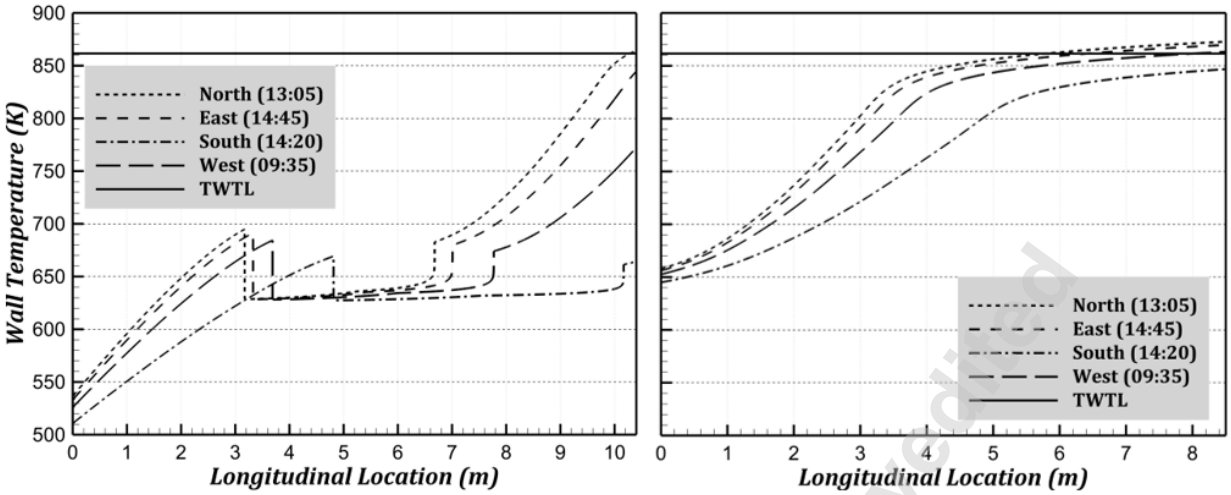

Fig. 20: Local profiles of tube wall temperature on the evaporator (left) and superheater sides (right)

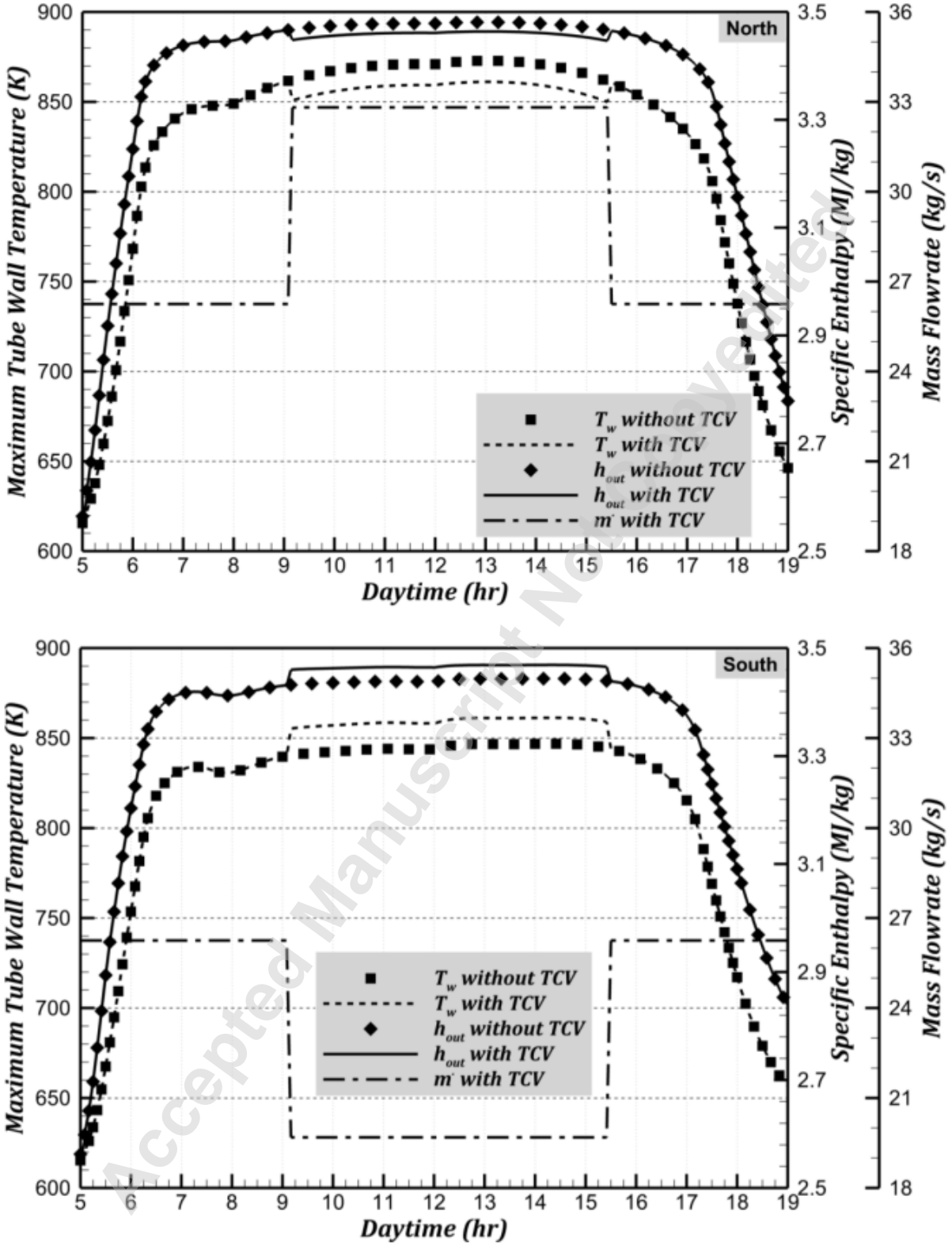

Fig. 21: Variation of maximum wall temperature, outlet specific enthalpy, and steam rate for the north (top) and south (bottom) sides of the superheater

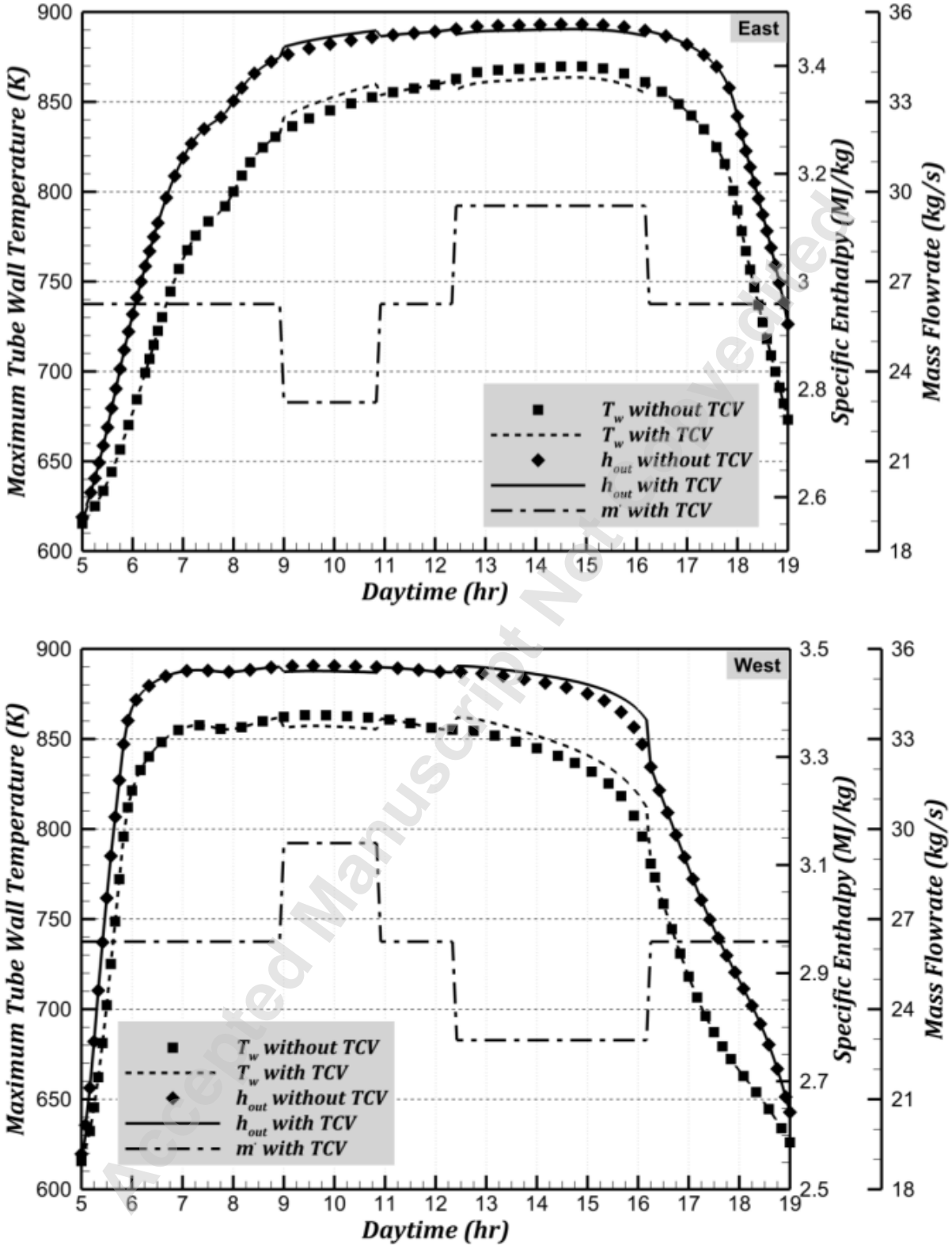

Fig. 22: Variation of maximum wall temperature, outlet specific enthalpy, and steam rate for the east (top) and west (bottom) sides of the superheater

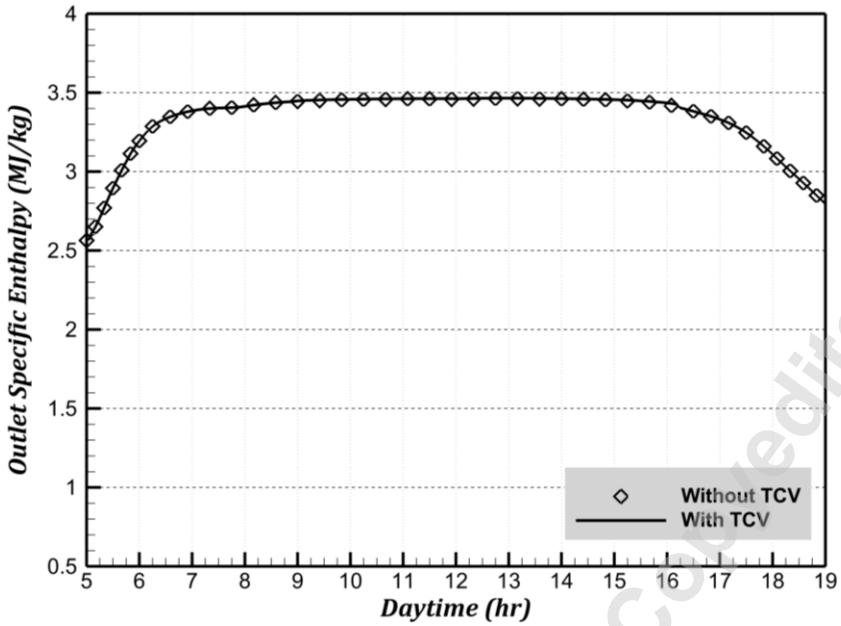

Fig. 23: Comparison of the specific enthalpy of steam generated by the superheater with or without utilizing a TCV